

# The crustal structure of the Dead Sea Transform

DESERT Group, M. Weber,<sup>1,5\*</sup> K. Abu-Ayyash,<sup>2</sup> A. Abueladas,<sup>2</sup> A. Agnon,<sup>3</sup> H. Al-Amoush,<sup>1</sup> A. Babeyko,<sup>1,11</sup> Y. Bartov,<sup>4</sup> M. Baumann,<sup>5</sup> Z. Ben-Avraham,<sup>6</sup> G. Bock,<sup>1</sup> J. Bribach,<sup>1</sup> R. El-Kelani,<sup>7</sup> A. Förster,<sup>1</sup> H.-J. Förster,<sup>5</sup> U. Frieslander,<sup>8</sup> Z. Garfunkel,<sup>3</sup> S. Grunewald,<sup>1</sup> H. J. Götze,<sup>9</sup> V. Haak,<sup>1</sup> Ch. Haberland,<sup>1</sup> M. Hassouneh,<sup>2</sup> S. Helwig,<sup>10</sup> A. Hofstetter,<sup>8</sup> K.-H. Jäckel,<sup>1</sup> D. Kesten,<sup>1</sup> R. Kind,<sup>1</sup> N. Maercklin,<sup>1</sup> J. Mechie,<sup>1</sup> A. Mohsen,<sup>1</sup> F. M. Neubauer,<sup>10</sup> R. Oberhänsli,<sup>5</sup> I. Qabbani,<sup>2</sup> O. Ritter,<sup>1</sup> G. Rumpker,<sup>1</sup> M. Rybakov,<sup>8</sup> T. Ryberg,<sup>1</sup> F. Scherbaum,<sup>5</sup> J. Schmidt,<sup>1</sup> A. Schulze,<sup>1</sup> S. Sobolev,<sup>1,11</sup> M. Stiller,<sup>1</sup> H. Thoss,<sup>1</sup> U. Weckmann<sup>1</sup> and K. Wylegalla<sup>1</sup>

<sup>1</sup>GeoForschungsZentrum, Potsdam, Germany

<sup>2</sup>Natural Resources Authority, Amman, Jordan

<sup>3</sup>Hebrew University, Jerusalem, Israel

<sup>4</sup>National Ministry of Infrastructure, Jerusalem, Israel

<sup>5</sup>University of Potsdam, Germany

<sup>6</sup>Tel Aviv University, Israel

<sup>7</sup>An-Najah National University, Nablus, Palestine

<sup>8</sup>Geophysical Institute of Israel, Lod, Israel

<sup>9</sup>Free University of Berlin, Germany

<sup>10</sup>University of Köln, Germany

<sup>11</sup>Institute of Earth Physics, Moscow

Accepted 2003 September 24. Received 2003 September 12; in original form 2003 May 20

## SUMMARY

To address one of the central questions of plate tectonics—How do large transform systems work and what are their typical features?—seismic investigations across the Dead Sea Transform (DST), the boundary between the African and Arabian plates in the Middle East, were conducted for the first time. A major component of these investigations was a combined reflection/refraction survey across the territories of Palestine, Israel and Jordan. The main results of this study are: (1) The seismic basement is offset by 3–5 km under the DST, (2) The DST cuts through the entire crust, broadening in the lower crust, (3) Strong lower crustal reflectors are imaged only on one side of the DST, (4) The seismic velocity sections show a steady increase in the depth of the crust-mantle transition (Moho) from ~26 km at the Mediterranean to ~39 km under the Jordan highlands, with only a small but visible, asymmetric topography of the Moho under the DST. These observations can be linked to the left-lateral movement of 105 km of the two plates in the last 17 Myr, accompanied by strong deformation within a narrow zone cutting through the entire crust. Comparing the DST and the San Andreas Fault (SAF) system, a strong asymmetry in subhorizontal lower crustal reflectors and a deep reaching deformation zone both occur around the DST and the SAF. The fact that such lower crustal reflectors and deep deformation zones are observed in such different transform systems suggests that these structures are possibly fundamental features of large transform plate boundaries.

**Key words:** crustal structure, Dead Sea, Middle East, shear zones, tectonics, transform faults.

## 1 INTRODUCTION

The processes responsible for large continental-scale shear zones, key elements of plate tectonics, and their relation and interaction

with the crust and upper mantle are still not fully understood, despite numerous efforts to study large transform systems, especially at the San Andreas Fault (SAF) system (Li *et al.* 1990; Brocher *et al.* 1994; Holbrook *et al.* 1996; Henstock *et al.* 1997; Unsworth *et al.* 1997; Ryberg & Fuis 1998; Fuis *et al.* 2001; Hole *et al.* 2001). The Dead Sea Transform (DST) (Fig. 1) has for a long time been considered a prime site to examine large shear zones (Quennell

\*Corresponding author: GFZ, Telegrafenberg, 14473 Potsdam, Germany. E-mail: mhw@gfz-potsdam.de

a

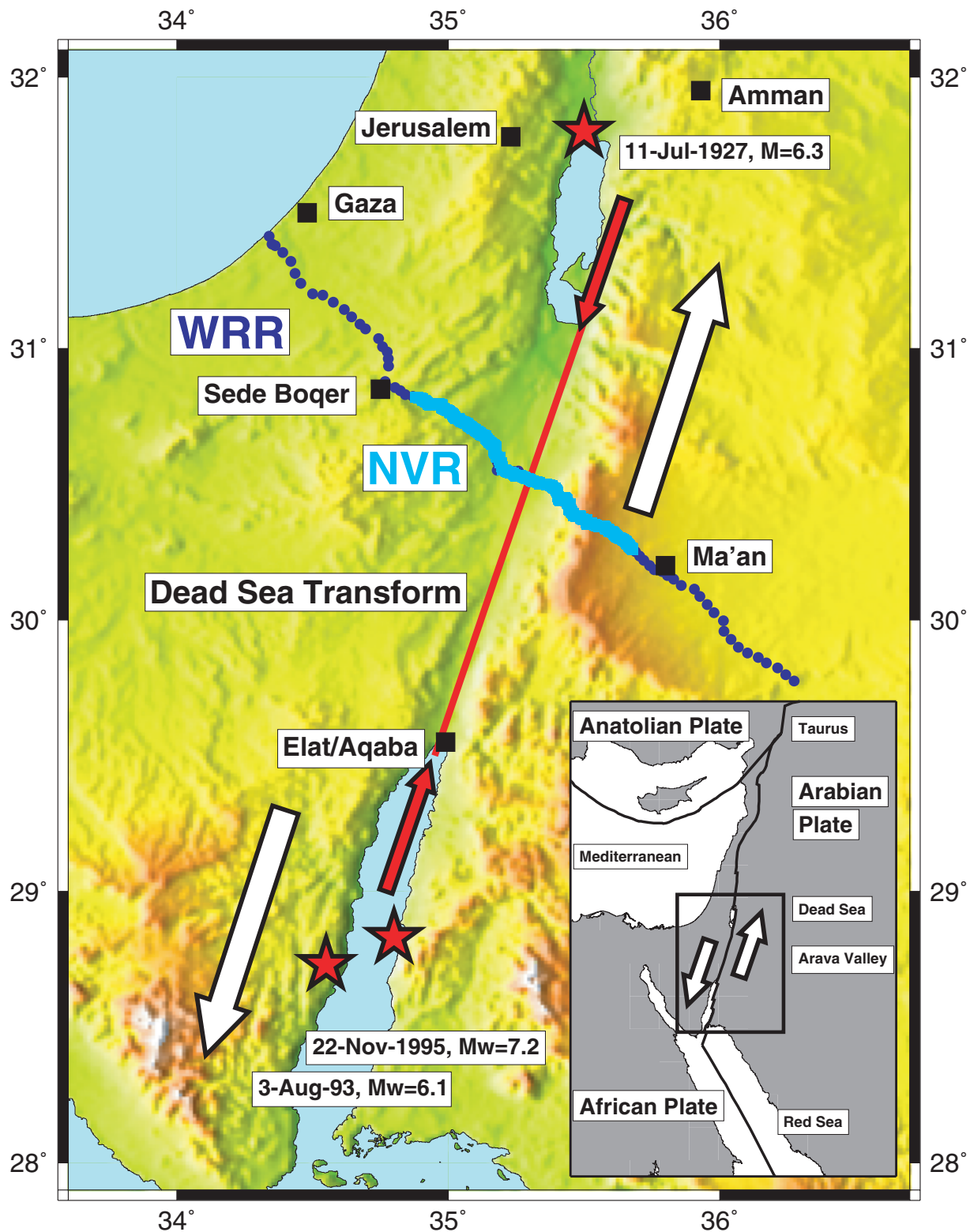


**Figure 1.** (a) Seismic experiments in the Middle East. The 260 km long wide-angle reflection/refraction profile (WRR, dark blue dots) crosses Palestine, Israel and Jordan. The near-vertical seismic reflection profile (NVR, cyan) coincides with the inner 100 km of the WRR. A red line and two red arrows indicate the Dead Sea Transform (DST) between the Dead Sea and the Red Sea. The white arrows indicate the left-lateral motion of 105 km between the African and Arabian plates. Red stars mark large earthquakes. (Inset) Tectonic setting of the DST. (b) Previous wide-angle reflection / refraction experiments in the study area (dashed black; Ginzburg *et al.* 1979a; Ginzburg *et al.* 1979b; Makris *et al.* 1983; El-Isa *et al.* 1987) together with the WRR profile of DESERT (blue) and the DST (red). The black circles are boreholes used in the interpretation (HD = Helez Deep-1A, MQ = Maktesh-Qatan, R1 = Ramon-1, EJ = El-Jafir-1).

b

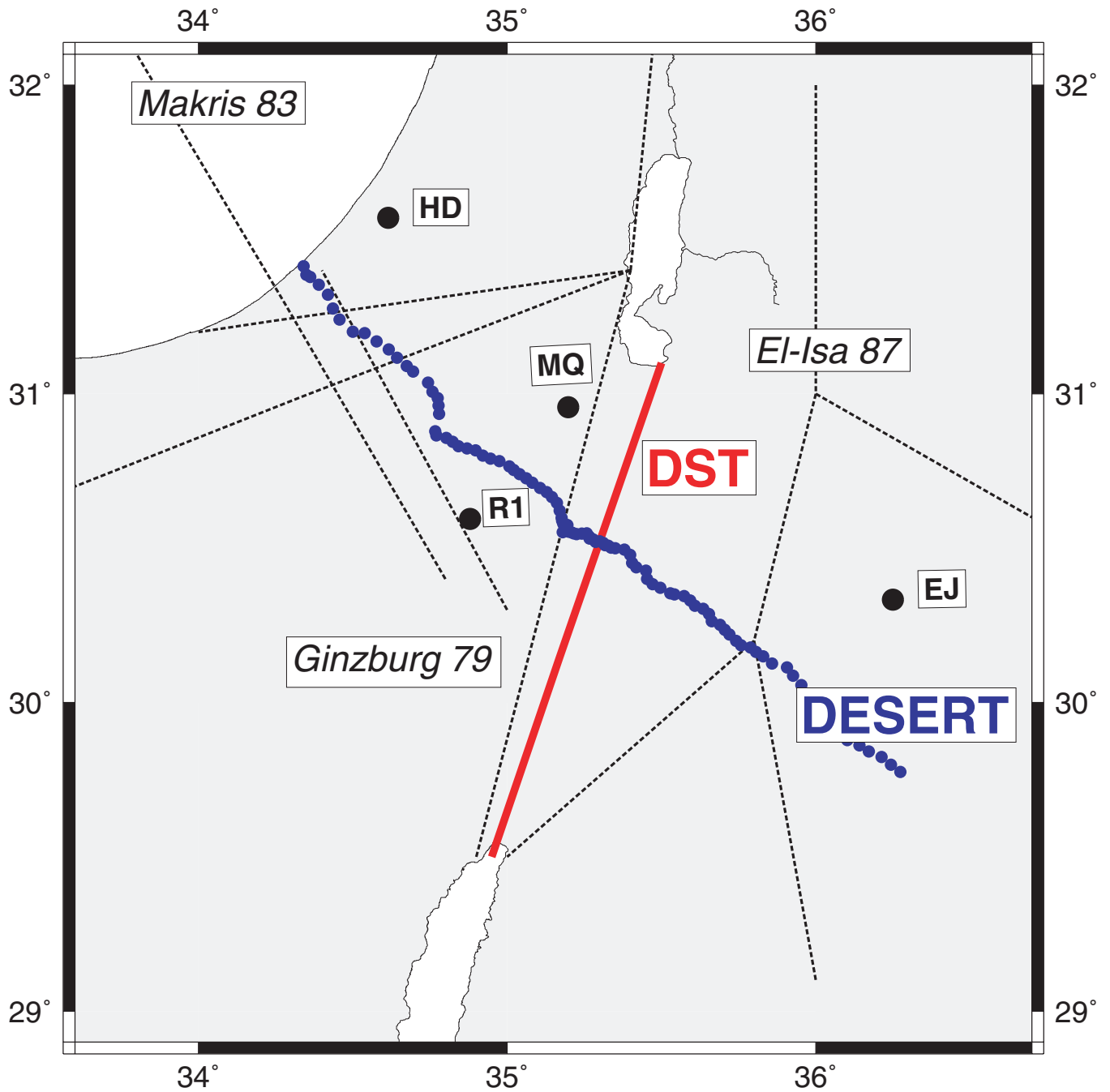
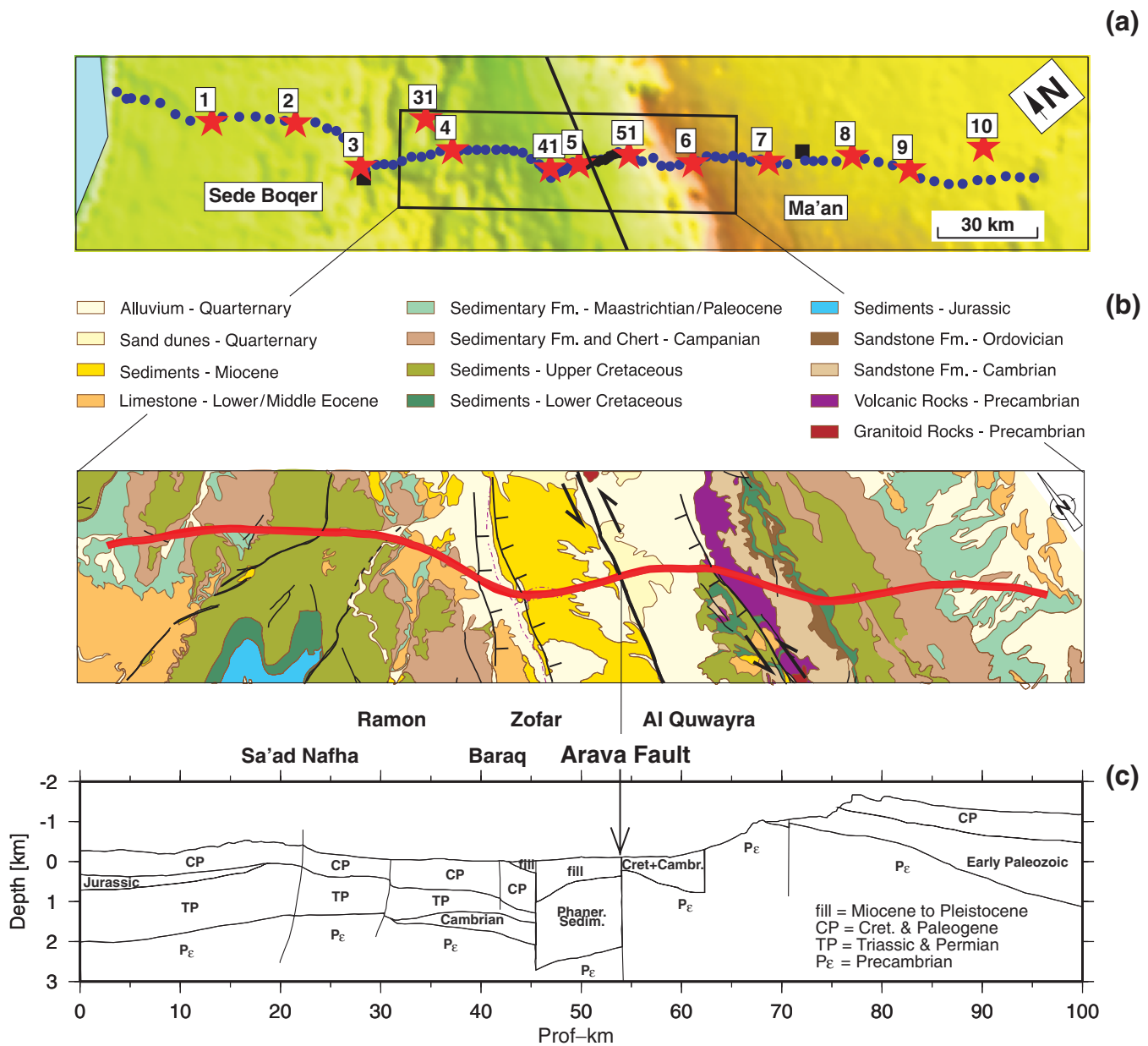


Figure 1 – continued

1958; Wilson 1965), but no crustal-scale geo-scientific investigation had been conducted across the DST until recently. This was due to the political situation in this area and the fact that the DST is situated in the border region between Israel and Jordan. Studies of historical earthquakes of the past few thousand years (Garfunkel *et al.* 1981; Amiran *et al.* 1994), palaeoseismic studies (Klinger *et al.* 2000; Kentor *et al.* 2001) and instrumental earthquake studies demonstrate that a number of damaging earthquakes have occurred along the

DST. The DST therefore also poses a considerable seismic hazard to Palestine, Israel and Jordan.

Here we present results of seismic investigations along a 260 km long transect (DESERT, DEAd SEa Rift Transect, Figs 1 and 2) extending from the Mediterranean coast to the Arabian platform. The central part of the transect crosses the DST at a location in the Arava Valley which is as far away as possible from the Dead Sea, a pull-apart basin, and the Red Sea, where active rifting occurs, and



**Figure 2.** (a) Location map for the WRR experiment. During the experiment 13 shots (red stars) were executed and recorded by 99 three-component instruments (blue dots) spaced 1–4.5 km apart along the whole length of the profile and 125 vertical component geophone groups (black dots between shots 5 and 51) with 100 m spacing along a 12.5 km long section of the profile in the Arava Valley. (b) Simplified geological map of the NVR profile area (modified after Sneh *et al.* 1998; Bartov *et al.* 1998). The red line is the smoothed reflection line of the NVR experiment. Six dominant faults (Saad Nafha, Ramon, Baraq, Zofar, Arava, Al Quwayra) are indicated in black. (c) Geological cross-section along the NVR profile. The arrow indicates the Arava Fault (AF), the dominant fault of the DST.

thus allows study of the DST and the tectonic processes controlling it in their most undiluted form. The apparent relative simplicity of the DST in the Arava Valley, and its relatively slow plate motion of  $\sim 0.5 \text{ cm yr}^{-1}$ , puts it in marked contrast to other large fault systems such as the North Anatolian Fault System, which is located amidst an orogenic belt (Sengör 1979) and the San Andreas Fault (SAF) system which originated from a complicated interaction between oceanic subplates and an accreted continental margin and has a fast relative plate motion of  $\sim 3.5 \text{ cm yr}^{-1}$  (see e.g. Holbrook *et al.* 1996; Henstock *et al.* 1997).

The fieldwork for our study was carried out in spring 2000 (DESERT Team 2000) by a team of scientists from Germany, Is-

rael, Jordan and Palestine. The components of DESERT that are reported in this paper are a near-vertical seismic reflection profile (NVR) and a seismic wide-angle reflection/refraction profile (WRR) (Figs 1 and 2). The seismic results are then the input and the reference for the thermo-mechanical modelling (Sobolev, unpublished data) and compared with the results from the San Andreas Fault system, which is one of the few other locations where similar experiments have been performed.

Central questions addressed in this study are:

- (1) What is the crustal structure at the DST in the Arava Valley?
- (2) Does the DST cut through the whole crust?

(3) Does rifting/extension play an important role in the dynamics of the DST?

(4) Are there structural similarities between the DST and the SAF system despite their different geological history and setting?

### Tectonic setting and geology along the profile

The DST is a system of left-lateral strike-slip faults that accommodate the relative motion between the African and Arabian plates. Except for a mild compressional deformation starting about 80 Ma, the larger Dead Sea region has remained a stable platform since the early Mesozoic. Approximately 17 Ma, this tectonic stability was interrupted by the formation of a transform, the DST, with a total left-lateral displacement of 105 km until today (Quennell 1958; Freund *et al.* 1970; Garfunkel 1981).

The crystalline basement of the area represents the NW part of the Arabo-Nubian Shield (ANS) and consists of mainly juvenile Late Proterozoic rocks (Stoeser & Camp 1985; Stern 1994). Regarding both isotopic and chemical data of xenoliths, the involvement of older crustal material in the lower crust of the ANS seems improbable (Henjes-Kunst *et al.* 1990; Stern 1994; Ibrahim & McCourt 1995). There is a gradual transition from the continental crust of the ANS with thicknesses of 35–40 km (El-Isa *et al.* 1987; Makris *et al.* 1983; Al-Zoubi & Ben-Avraham 2002) to the crust of the eastern Mediterranean, that is assumed to be partly underlain by typical oceanic crust with thicknesses smaller than 10 km (Ginzburg *et al.* 1979a; Makris *et al.* 1983; Ben-Avraham *et al.* 2002), see also Fig. 1(b).

The Precambrian basement is usually overlain by an Infracambrian to Early Cambrian volcano-sedimentary succession of variable thickness. Whereas coarse-grained clastics (Saramuj and Elat conglomerates) are restricted to fault-bounded basins, fine-grained clastics, mostly consisting of arkosic sandstones and associated volcanic rocks (Zenifim Formation, Haiyala Volcaniclastic Unit and equivalent rock units) have been observed in large parts of the Israel and Jordan subsurface (Weissbrod & Sneh 2002). In boreholes close to the WRR and NVR profiles (Fig. 1b) the Zenifim Formation was determined to be several hundreds of metres thick (> 500 m in Maktesh-Qatan, MQ, and >2000 m in Ramon-1, R1), although its base has not been encountered in any of the Israeli boreholes.

The position of the study region at the NW edge of the ANS, i.e. at a passive continental margin since early Paleozoic times, is reflected in facies changes and varying sedimentary thicknesses along the seismic profiles (Fig. 2). The Phanerozoic along the northwestern part of the profile is dominated by Cretaceous and Tertiary rocks underlain by Jurassic, Triassic and Permian sequences that thin out towards the east. East of the DST, however, Permian to Triassic strata are missing and Lower Cretaceous rocks unconformably overlie Ordovician and Cambrian sandstones. The crystalline basement rocks (calc-alkaline granitoids and rhyolites) cropping out in the Jebel Humrat Fiddan area east of the DST are thought to be equivalent to the basement rocks of the Timna region in Israel, near Elat.

### Previous seismic work in this area

Previous crustal-scale wide-angle reflection/refraction experiments in the study area (Fig. 1b) include that in Israel in 1977 (Ginzburg *et al.* 1979a), the onshore-offshore experiment between the northwestern end of the WRR profile and Cyprus in 1978 (Makris *et al.* 1983; Ben-Avraham *et al.* 2002) and that in Jordan in 1984 (El-Isa *et al.* 1987). However, there was no profile, which crossed the DST

to provide a complete image across this structure. Moreover, deep seismic reflection data only exist from the area between the Dead Sea and the Mediterranean (Yuval & Rotstein 1987; Rotstein *et al.* 1987), and high-resolution seismics (Frieslander 2000) are mostly limited to the western part of the Arava Valley. Further south within the Afro-Arabian rift system seismic profiles, which cross the rift structures, have proved to be very useful to understand the crustal structure as, for example, the E-W profiles crossing the Kenya rift (Maguire *et al.* 1994; Braile *et al.* 1994; Birt *et al.* 1997). Seismic crustal investigations of the Afro-Arabian Rift system are summarized by Mechie & Prodehl (1988) and Prodehl *et al.* (1997).

## 2 NEAR-VERTICAL INCIDENCE REFLECTION EXPERIMENT

The near-vertical incidence reflection (NVR) experiment was carried out during March 2000. It coincides with the inner 100 km of the WRR profile crossing the Arava Fault (AF), the main fault of the southern DST system, in the Arava Valley almost perpendicularly (Fig. 1). It aims to reveal the crustal architecture down to the crust-mantle discontinuity (the Moho) and to resolve the main fault geometry. A vibroseis survey with heavy energy penetration, dense Common Depth Point (CDP) spacing and high subsurface coverage was used. A few explosive shots with single-fold coverage along the line were additionally fired in order to get reflections from the deeper crust, the Moho and possibly from the upper mantle.

NVR data processing was carried out in a step-by-step and strictly data-dependent manner, i.e. processing parameters have been analysed and controlled at numerous positions along the line. Nevertheless, deep-seismic processing is not a standard tool since its methods and results are highly parameter-dependent. To ease the reading of this paper some methodical aspects on the processing from raw data to the final migrated line-drawing section, the main result of the NVR experiment, are described in more detail in Appendix A.

## 3 WIDE-ANGLE REFLECTION/REFRACTION EXPERIMENT

### 3.1 WRR experiment configuration

The wide-angle reflection/refraction (WRR) experiment was completed between 2000 February 9 and 27. The NW–SE trending, 260 km long profile (Figs 1 and 2), which passed through Palestine, Israel and Jordan, crossed the Arava Fault at about 70 km south of the southern end of the Dead Sea. During the experiment 13 shots, including two quarry blasts, were executed within three days. The quarry blasts (shot nos. 10 and 31 in Fig. 2a) had charge sizes of 8500 kg and 12 000 kg respectively. Of the 11 borehole shots, five were large shots (shot nos. 1, 3, 5, 7 and 9 in Fig. 2a) with charge sizes of 720–950 kg. They were executed with the aim of obtaining the whole crustal structure and, in particular, the wide-angle reflection from the Moho. The other six shots (shot nos. 2, 4, 41, 51, 6 and 8 in Fig. 2a) were small shots with charge sizes of 30–80 kg. They were executed with the aim of obtaining the detailed structure of the top of the seismic basement. The 13 shots were recorded by 99 three-component instruments spaced 1–4.5 km apart along the whole length of the profile and 125 vertical component geophone groups with 100 m spacing along a 12.5 km long section of the profile between shots 5 and 51 in the Arava Valley (Fig. 2a). The

three-component instruments were placed 1 km apart in the Arava Valley and 4–4.5 km apart at the ends of the profile. On the shoulders of the Arava Valley, where the Moho reflection from beneath the Arava Valley was expected to be well recorded at around the critical distance, the three-component instruments were spaced about 2.5 km apart. The decision to deploy the three-component instruments closest together in the Arava Valley as well as to deploy the 125 vertical geophone groups here proved, in hindsight, to be correct as it greatly helped the phase correlations in this important area with difficult recording conditions due to the high ambient noise level. Logistic considerations determined that the 125 vertical geophone groups only be deployed in Jordan.

### 3.2 WRR data and phase correlations

Figs 3 to 9 show, for each of the seven large shots including the two quarry blasts along the WRR profile, the compressional ( $P$ ) seismic wave field recorded by the vertical component of the instruments at each receiver position. These shot gathers are displayed in the form of distance versus reduced-time record sections, in which each trace has been band pass filtered (2–20 Hz) and normalized with respect to its own maximum amplitude. The data recorded by the 99 three-component instruments along the whole profile are shown for all seven large shots (Figs 3a, 4a, 5, 6, 7, 8a and 9a). The data recorded by the 125 vertical geophone groups, along the 12.5 km long section of the profile in the Arava Valley, are shown for the four shots from which the deeper intra-crustal reflections ( $PiP$ ) and the Moho-reflections ( $PmP$ ) were obtained in addition to the first arrival refractions ( $Pg$ ) through the upper crust (Figs 3b, 4b, 8b and 9b). The record sections, which are not displayed, are those, which only show recordings of the  $Pg$  phase (Table 1).

Three major seismic phases can be correlated in the record sections and have been used to derive the  $P$ -wave velocity model. The first,  $Pg$ , is observed in the record sections from all shot-points (Table 1). In the record sections from some of the large shots it can be observed out to distances of about 175 km (Figs 5 and 9a). Over the first few tens of kilometres distance in the record sections, the phase can be split into two distinct branches, each with an apparent velocity significantly less than  $6 \text{ km s}^{-1}$ . The first branch out to distances of 5–10 km generally has apparent velocities between  $3.0$  and  $4.0 \text{ km s}^{-1}$  while the second branch between distances of 5–10 km and 10–25 km generally has apparent velocities between  $4.5$  and  $5.5 \text{ km s}^{-1}$ . The data from the previous experiments in the study area also generally indicated two distinct first arrival branches at near offsets with apparent velocities less than  $6 \text{ km s}^{-1}$  (Ginzburg *et al.* 1979a; El-Isa *et al.* 1987). Beyond the first few tens of kilometres distance in the record sections, the phase has average apparent velocities, which are generally in the range  $6.0$ – $6.25 \text{ km s}^{-1}$ . In the record sections from shots 1 and 3, the densely spaced data from the Arava Valley aid the correlation of the  $Pg$  phase out to distances of 115 and 73 km respectively east of the shot-points (Figs 3b and 4b). To the west of both shot-points, apparent velocities of around  $6.0 \text{ km s}^{-1}$  are not observed due to the high ambient noise level at relatively short distances from the shot-points. However, from the powerful quarry blast (shot 31), an apparent velocity of about  $6.0 \text{ km s}^{-1}$  is observed to the west of the shot-point (Fig. 5). To the east of shot 31,  $Pg$  arrivals can be recognized out to about 100 km distance and then beyond 140 km distance. From shot 5, the large shot within the Arava Valley,  $Pg$  arrivals can be observed out to 50–60 km distance on both sides of the shot-point and there are also a few  $Pg$  arrivals at 80–90 km distance east of the shot (Fig. 6). From the

large shots 7, 9 and 10 on the eastern side of the Arava Valley,  $Pg$  arrivals can be observed out to the eastern end of the profile from all three shot-points (Figs 7, 8a and 9a). To the west, the  $Pg$  arrivals can be recognized out to the position of shot 3 in each of the record sections. Beyond this point the ambient noise levels become too high. Again the densely spaced data from the Arava Valley aid the correlation of the  $Pg$  phase, especially for shot 10 at distances of 102–114 km (Fig. 9b).

The second major phase, which can be recognized on the record sections from the large shots, is  $PiP$ , the intra-crustal reflection from the boundary between the upper and lower crust. This phase is observed in the record sections from two of the large shots, 1 and 31, on the western side and two of the large shots, 7 and 9, on the eastern side of the Arava Valley. From two of the shots, 1 and 9, the phase can be recognized with a good degree of consistency, often from trace to trace, in the densely spaced data from the Arava Valley (Figs 3b and 8b). In the record section from the three-component data from shot-point 9, the phase can be followed, in part due to a significant increase in amplitude, out to about 140 km distance (Fig. 8a). From the other two shot-points, 31 and 7, the phase is defined by seven arrivals in each record section (Figs 5 and 7). These arrivals are, in part, marked due to the amplitude increase associated with the onset. The fact that an intra-crustal reflected phase has also been recognized at similar distances and traveltimes in the data from previous experiments in the study area (Ginzburg *et al.* 1979b; Perathoner 1979; El-Isa *et al.* 1987), gives additional confidence to the identification of the intra-crustal reflection along the WRR profile.

The third major phase, which is observed in the record sections from the seven large shots, is  $PmP$ , the reflection from the Moho.  $Pn$ , the refracted phase through the uppermost mantle, was not recognized in the data from the WRR profile. However, in the data from previous experiments in the study area  $Pn$  was observed in association with  $PmP$  (Ginzburg *et al.* 1979a; Ginzburg *et al.* 1979b; El-Isa *et al.* 1987). The fact that  $PmP$  was observed at similar distances and traveltimes in the data from previous experiments in the study area gives additional confidence that the phase identified as  $PmP$  along the WRR profile, actually is the Moho reflection. The  $PmP$  phase, which occurs in the distance range from 70–160 km, can be well correlated, often from trace to trace, in the densely spaced data from the Arava Valley (Figs 3b, 4b, 8b and 9b). From these data the phase can then be followed to larger and/or smaller distances in the three-component data from these four shots (Figs 3a, 4a, 8a and 9a). The phase can also be recognized in the three-component data from the other three shots, 31, 5 and 7 (Figs 5–7). In some cases e.g. shots 7 and 9 (Figs 7 and 8a), the  $PmP$  phase can be recognized not so much by sharp onsets but rather by an increase in energy level. In the record section from shot 10 (Fig. 9a), the correlation of the  $PmP$  phase at 120–140 km distance is impeded due to a secondary phase which mimics the  $Pg$  phase about 1.7 s later and which is thus most probably a source effect. Neither the  $PmP$  nor the  $PiP$  phases can be observed to the west of shot-point 3, due to high ambient noise levels in this area.

In addition to the three major phases, it is possible that there is an additional intra-crustal reflection,  $Pi2P$ , between the  $PiP$  and the  $PmP$  phases. 22 onsets were observed for this possible phase in the three-component data from four of the shots, 3, 31, 5 and 9 (Figs 4a, 5, 6 and 8a). However, for the following reasons the preferred model, described below, does not include a boundary associated with this possible phase. First, only a few arrivals for this possible phase were identified. Second, this possible phase was not convincingly observed in the densely spaced data from the Arava Valley from shots

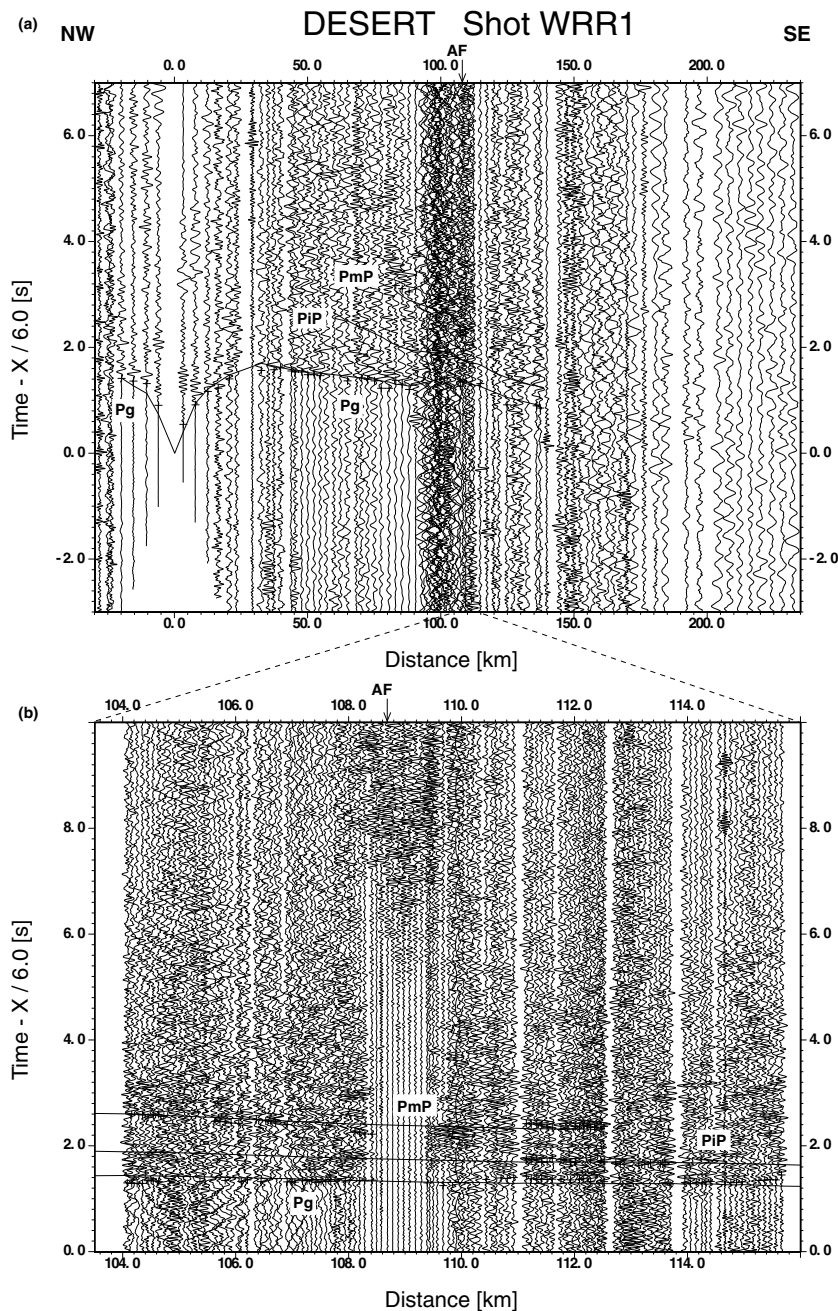


**Figure 3.** Seismic data from shot 1 recorded along the wide-angle reflection/refraction (WRR) profile. (a) Record section shows the vertical component of  $P$ -wave motion from the three-component instruments along the whole length of the profile. (b) Record section shows the densely spaced data recorded by the 125 vertical geophone groups along the 12.5 km long segment of the profile in the Arava Valley. Both record sections are reduced with a velocity of  $6 \text{ km s}^{-1}$  and each trace is normalized individually and band-pass filtered from 2–20 Hz. Lines represent phases calculated from the model in Fig. 11(a), while crosses represent observed traveltimes. Key:  $P_g$ —first arrival refraction through the upper crust,  $P_iP$ —reflection from the top of the lower crust,  $P_mP$ —Moho reflection, AF—Arava Fault.

3 and 9 (Figs 4b and 8b). In the case of shot 3, this possible phase should be expected to be clearly observed at about 3.4 s reduced-time in the densely spaced data, as these data are at similar distances to those at which the onsets are observed in the three-component data. In the case of shot 9, the densely spaced data are only at distances of about 10 km less than those at which the onsets are observed in the three-component data. Third, such a phase was not recognized in any of the record sections from previous experiments in the study area (Ginzburg *et al.* 1979a; Ginzburg *et al.* 1979b; El-Isa *et al.* 1987).

### 3.3 WRR modelling

In order to interpret the phase correlations described above, the arrival times of the various phases were first picked and 1-D velocity-depth models were constructed for each shot in each of the two directions using both traveltimes and amplitudes. These 1-D models were then combined to provide starting models of varying degrees of complexity, for the derivation of a 2-D  $P$ -wave velocity model. The 1-D velocity-depth models were calculated using trial-and-error forward modelling in which theoretical traveltimes were calculated

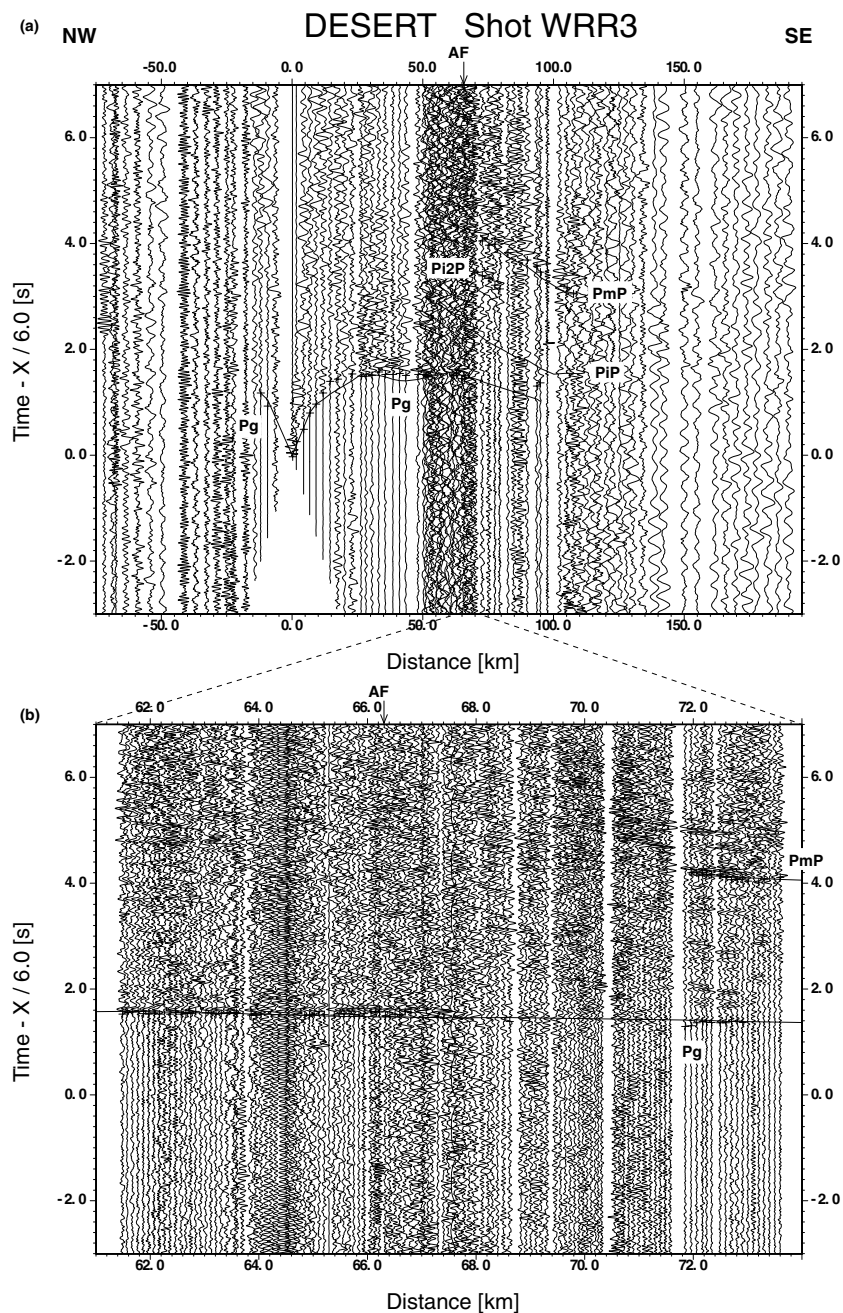


**Figure 4.** Seismic data from shot 3 recorded along the WRR profile. (a) Record section shows the vertical component of  $P$ -wave motion from the three-component instruments along the whole length of the profile. (b) Record section shows the densely spaced data recorded by the 125 vertical geophone groups along the 12.5 km long segment of the profile in the Arava Valley. The data are processed and presented as in Fig. 3. Key: see Fig. 3 and  $Pi2P$ —possible reflection from 30 km depth.

using ray-tracing (see, for example, Cerveny *et al.* 1977) and theoretical seismograms were calculated using the reflectivity method (Fuchs & Müller 1971). The 2-D model was derived mainly by inverse modelling of traveltimes supplemented by forward modelling of amplitudes. For the traveltime modelling, the forward problem was solved by classical ray tracing techniques (Cerveny *et al.* 1977) for the reflected phases, and finite-difference ray tracing based on the eikonal equation (Vidale 1988; Podvin & Lecomte 1991; Schneider *et al.* 1992) for the first arrival refracted phases. Partial derivatives of the calculated traveltimes with respect to the velocity and interface nodes were then derived using the techniques described by

Lutter & Nowack (1990), Lutter *et al.* (1990) and Zelt & Smith (1992). Subsequently, a damped least-squares inversion (see, for example Zelt & Smith 1992) was carried out to obtain updates for the velocity and interface nodes, and the forward and inverse problems were repeated until an acceptable convergence between the observed and calculated traveltimes was obtained. To supplement and guide the traveltime modelling, amplitudes were calculated using a finite-difference approximation of the wave equation for 2-D heterogeneous elastic media by Kelly *et al.* (1976) with transparent boundary conditions (Reynolds 1978) and implemented by Sandmeier (1990).

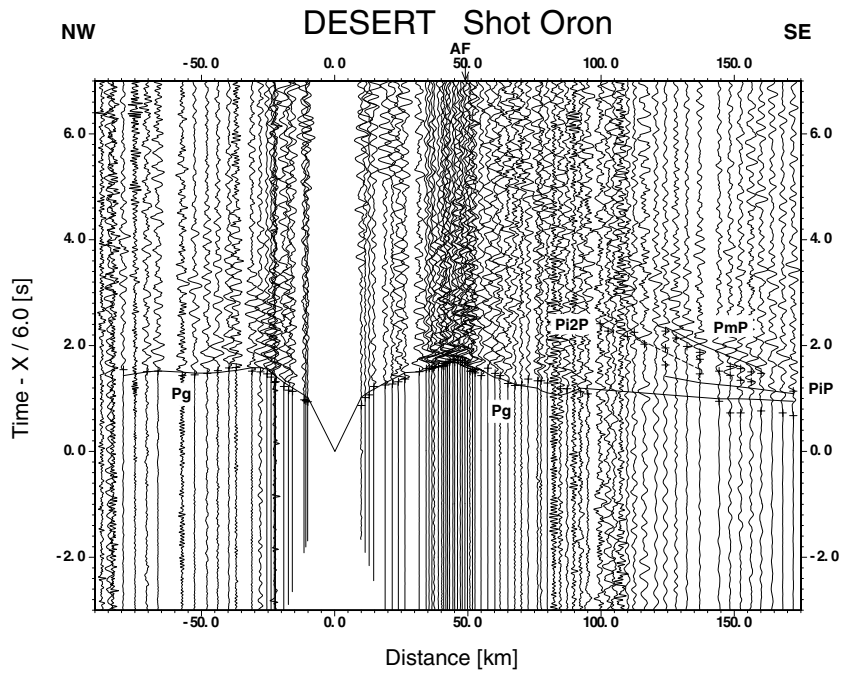


Figure 5. Seismic *P*-wave data from shot 31 (Oron quarry blast) recorded along the whole length of the WRR profile. The data are processed and presented as in Fig. 3(a). Key: see Figs 3 and 4.

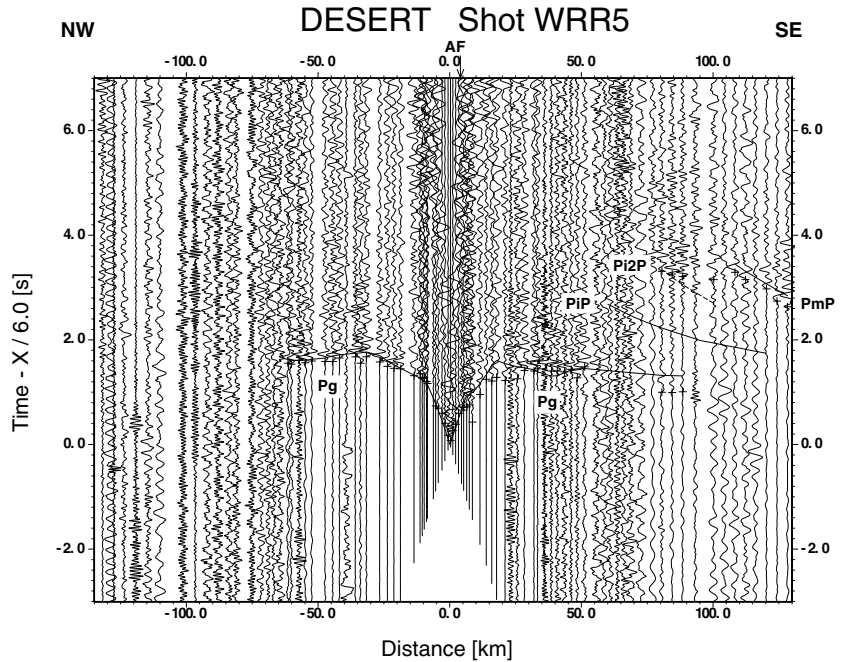
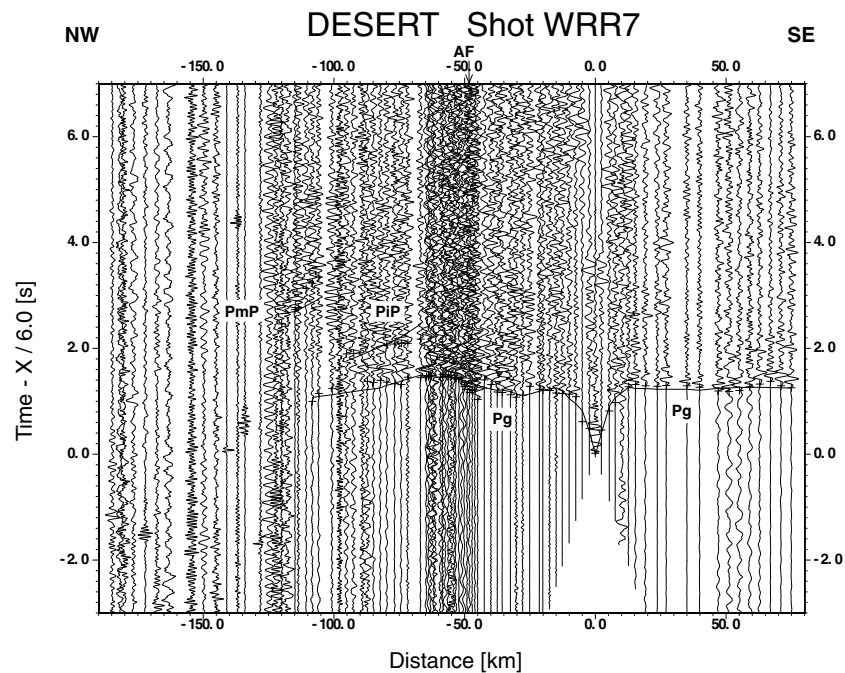


Figure 6. Seismic *P*-wave data from shot 5 recorded along the whole length of the WRR profile. The data are processed and presented as in Fig. 3(a). Key: see Figs 3 and 4.

The traveltimes modelling was carried out using a top-to-bottom approach in three major steps (upper crust, boundary between upper and lower crust, lower crust and Moho), as described below. In total, 1732 traveltimes readings were used in the inversion to derive the model (Table 1), and the model contains 26 independent velocity and interface depth parameters (Tables 2 and 3). Although the velocities and interface depths in the model were usually specified

at 10–50 km intervals along the profile, in the inversion a smaller number of independent velocity and depth parameters was solved for by grouping the individual nodes together (Table 2). As a consequence of the inversion, the resolution and standard errors for the various parameters can be calculated (Table 2). These standard error estimates should be viewed as lower bounds of the true errors (Zelt & Smith 1992). More realistic values are  $\pm 0.2 \text{ km s}^{-1}$  for the



**Figure 7.** Seismic  $P$ -wave data from shot 7 recorded along the whole length of the WRR profile. The data are processed and presented as in Fig. 3(a). Key: see Fig. 3.

velocities of the top two layers,  $\pm 0.1 \text{ km s}^{-1}$  for the velocity of the seismic basement (3rd layer),  $\pm 1 \text{ km}$  for the top two interfaces,  $\pm 2 \text{ km}$  for the top of the lower crust and  $\pm 3 \text{ km}$  for the Moho.

### Step 1: upper crustal structure

In the first step, 1331 first arrival traveltimes from the  $P_g$  phase (Table 1) were inverted in order to obtain the velocity structure of the top three layers and the structure of the two interfaces between these layers (Figs 10a and 11a). As mentioned above, the  $P_g$  phase can be divided into three distinct traveltime branches, with two of these branches having apparent velocities less than  $6 \text{ km s}^{-1}$  and the third having average apparent velocities of  $6.0\text{--}6.25 \text{ km s}^{-1}$ . Thus three layers, corresponding to the three distinct traveltime branches, and two interfaces between these layers were utilized to derive the upper crustal structure. As east of the Arava Valley, previous studies (El-Isa *et al.* 1987) have shown that the top layer corresponds to the Cenozoic–Mesozoic succession, the top layer in the starting model was thinned out and is absent between model km 176 and 188, where Palaeozoic or older rocks are exposed at the surface along the profile. As the number of arrival times defining the two  $P_g$  traveltime branches with apparent velocities less than  $6 \text{ km s}^{-1}$  is rather small, the starting model contained laterally varying velocities in the top two layers and laterally varying interface depths for the two interfaces between the top three layers, derived from the 1-D modelling. The starting model had uniform velocities of  $6.1$  and  $6.25 \text{ km s}^{-1}$  along the top and bottom surfaces respectively, of the third top layer. The velocities at the top and bottom of each individual layer were constrained to be updated by the same amount in each iteration of the inversion. In the inversion five independent depth nodes on the upper of the two interfaces and six independent depth nodes on the lower of the two interfaces, each with an *a priori* uncertainty estimate of  $\pm 3.0 \text{ km}$ , were used. In addition, two independent velocity nodes, one west of the AF and one east of the AF in each of the three layers, each with an *a priori* uncertainty estimate of  $\pm 0.5 \text{ km s}^{-1}$

were employed, making a total of 17 model parameters to be solved for (Tables 2 and 3).

After four iterations, the average absolute difference between the observed and theoretical traveltimes had decreased from  $0.17 \text{ s}$  to  $0.12 \text{ s}$  with no further significant improvement occurring. The average absolute traveltime difference of  $0.12 \text{ s}$  is thus just slightly larger than the standard deviation of  $0.10 \text{ s}$  for the traveltime readings. Thus the model does not try to overfit the data. The ray diagram (Fig. 10a) shows that, although only 446 of the 1331 rays are displayed, the region between the two outermost shots is well constrained, especially the lower of the two interfaces and the third top layer. Inspection of the resolution matrix shows that all nodes are well resolved and all off-diagonal elements of the resolution matrix are small compared to the diagonal elements.

The average velocity in the top layer varies laterally from  $3.1\text{--}3.7 \text{ km s}^{-1}$  along the profile while the thickness of the top layer reaches maximum values of about  $1.5 \text{ km}$  east of the Arava Valley, around  $2.2 \text{ km}$  within the Arava Valley and about  $2.5 \text{ km}$  west of the Arava Valley (Fig. 11a). The average velocity in the second top layer varies laterally from  $4.0 \text{ km s}^{-1}$  where this layer actually reaches the surface to  $5.1 \text{ km s}^{-1}$  west of the Arava Valley. The seismic basement occurs at depths of  $3\text{--}4 \text{ km}$  beneath the eastern shoulder of the Arava Valley, deepens to about  $7 \text{ km}$  as the AF is crossed in the Arava Valley, shallows to about  $6 \text{ km}$  below the western flank of the Arava Valley and then deepens westwards towards the coast. The top of the seismic basement has velocities of  $6.1\text{--}6.2 \text{ km s}^{-1}$  while the base of the upper crust has velocities of  $6.3\text{--}6.4 \text{ km s}^{-1}$ .

At least 15 other start models were tested in this step of the inversion. Some of these models were 1-D models and thus simpler than the one described above. Some of them had up to 37 model parameters, which is substantially more than possessed by the model described above. Many of the inversion runs had technical problems such as the development of models with interfaces crossing each other. None of their inversion runs resulted in such a low average

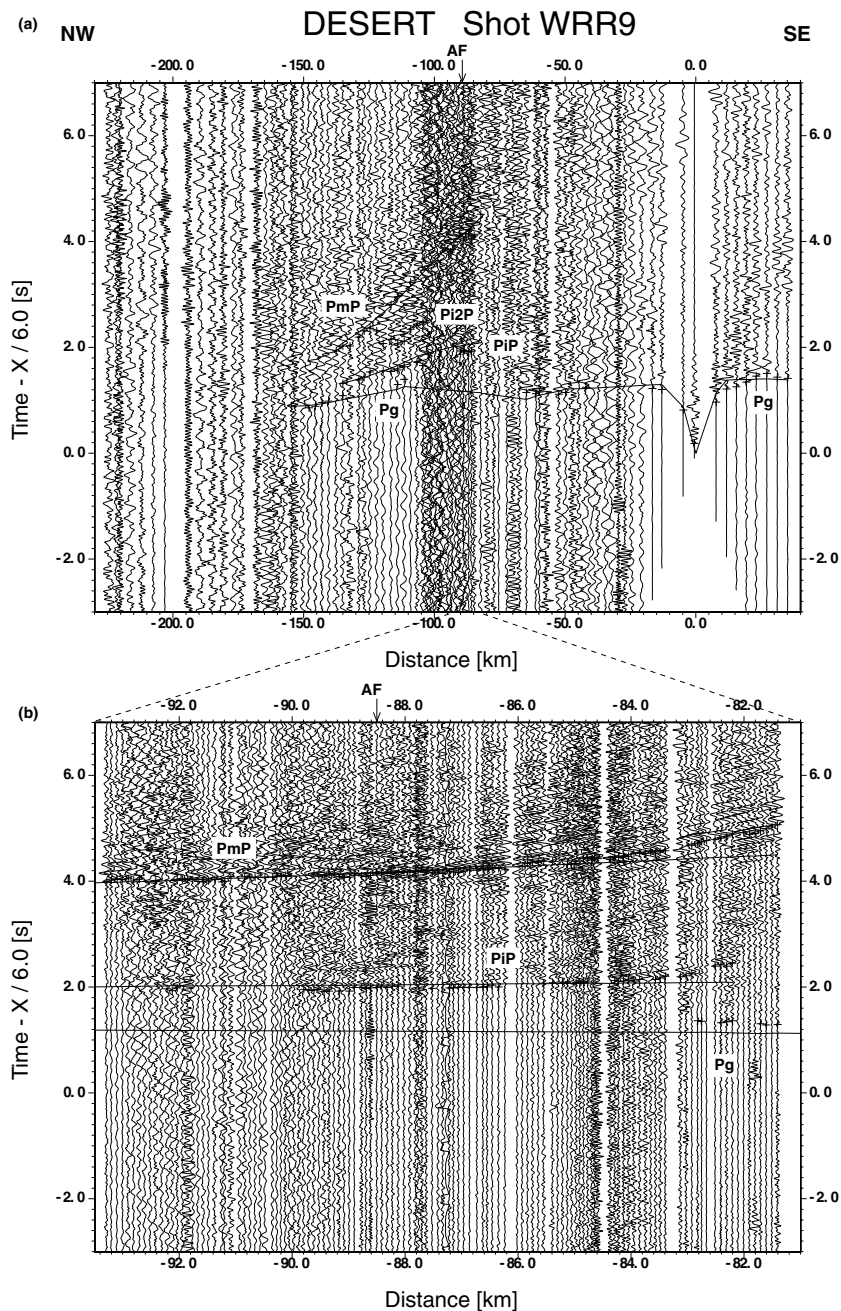


**Figure 8.** Seismic data from shot 9 recorded along the WRR profile. (a) Record section shows the vertical component of  $P$ -wave motion from the three-component instruments along the whole length of the profile. (b) Record section shows the densely spaced data recorded by the 125 vertical geophone groups along the 12.5 km long segment of the profile in the Arava Valley. The data are processed and presented as in Fig. 3. Key: see Figs 3 and 4.

absolute traveltimes difference. Some of the resulting models did not look geologically reasonable e.g. shallow basement beneath the coast at the NW end of the profile. Many resulting models did, however, show a rapid decrease in seismic basement depths to the east, as the AF is crossed and large depths to seismic basement beneath the Arava Valley and towards the coast at the NW end of the profile. These model tests give confidence that the model chosen here (Fig. 11a) is actually a good model.

At the NW end of the profile, the top of the seismic basement probably correlates with the top of the Precambrian. A borehole about 35 km NE of the NW end of the WRR profile (Helez Deep-1A, HD in Fig. 1b) shows the top of the Precambrian (schists) to be

at about 6 km depth. In Israel, SE of model km 100 (Figs 1b and 11a) boreholes (Ramon-1 (R1), Maktesh-Qatan (MQ); Weissbrod 1969; Garfunkel & Derin 1984; Hirsch & Picard 1988) close to the WRR profile show that the top of the seismic basement lies 2–3 km below the top of the Precambrian. In this area the upper part of the Precambrian succession consists of sediments and volcanic rocks of the Zenifim formation, which most probably have lower velocities than the seismic basement and which reach thicknesses of 2 km (see e.g. the Ramon borehole, Fig. 1b). The top of the seismic basement probably correlates with the top of the Precambrian intrusive igneous or metamorphic rocks. Where the velocities of such rocks have been measured where they are exposed at the surface in southwest

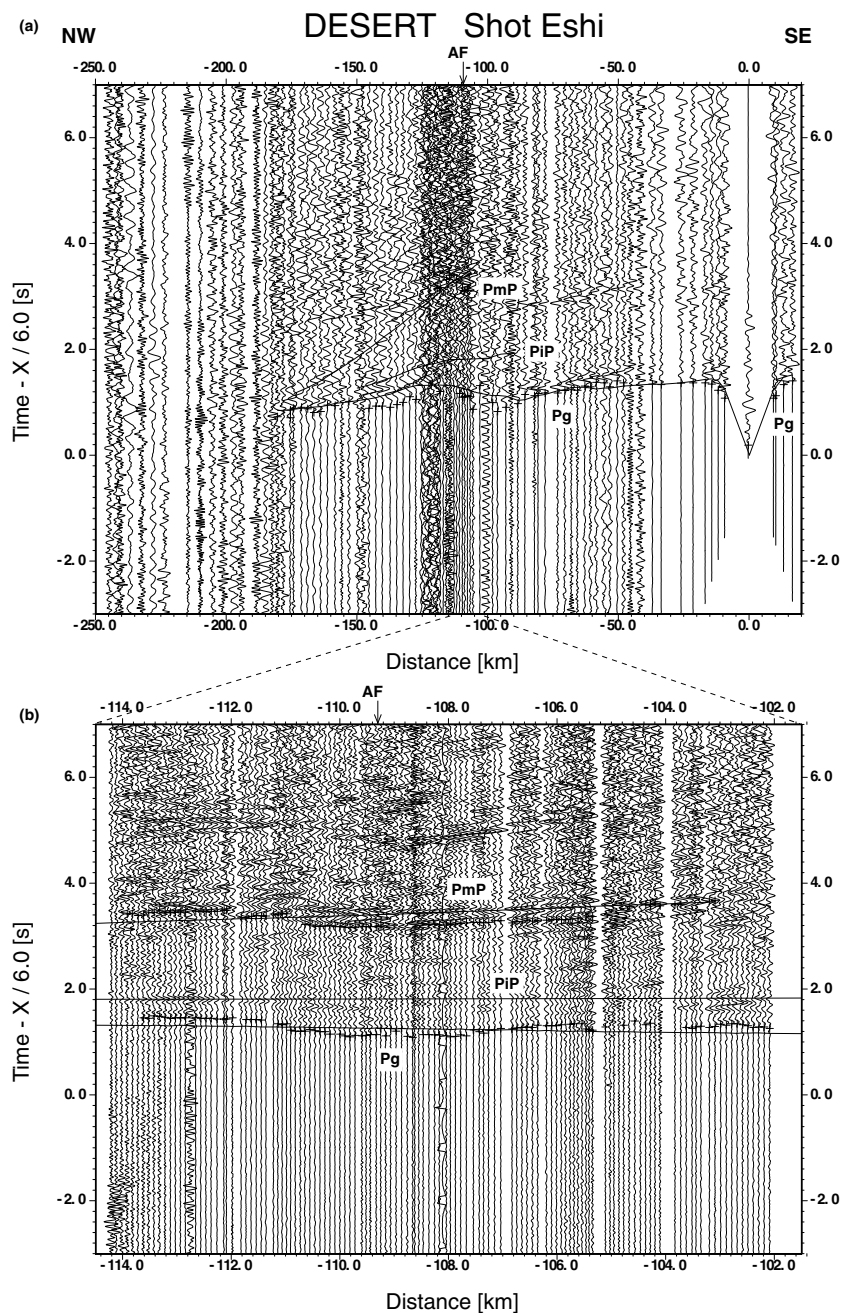


**Figure 9.** Seismic data from shot 10 (Eshidiyah quarry blast) recorded along the WRR profile. (a) Record section shows the vertical component of  $P$ -wave motion from the three-component instruments along the whole length of the profile. (b) Record section shows the densely spaced data recorded by the 125 vertical geophone groups along the 12.5 km long segment of the profile in the Arava Valley. The data are processed and presented as in Fig. 3. Note the secondary phase which mimics the  $P_g$  phase about 1.7 s later and which is thus most probably a source effect. Key: see Fig. 3.

Jordan, the values obtained were close to  $6 \text{ km s}^{-1}$  (El-Isa *et al.* 1987). This is in agreement with the velocities obtained for the top of the seismic basement beneath the WRR profile. To the SE of the AF, Precambrian volcanic rocks are exposed between model km 176 and 181. Further to the SE about 40 km NE of shot 8 (Fig. 2a) the El-Jafr-1 borehole (EJ in Fig. 1b) shows that Saramuj conglomerates of Precambrian age are reached at a depth of 3.3 km and continue down to the base of the hole at 4.0 km. Thus to the SE of the AF the top of the seismic basement also probably correlates with the top of the Precambrian intrusive igneous or metamorphic rocks.

## Step 2: mid-crustal boundary

In step 2 the depths of the boundary between the upper and lower crust were determined by inverting for 103 traveltimes readings of the  $PiP$  reflection (Table 1). The 2-D starting model consisted of a horizontal boundary at about 22 km depth. Three independent boundary nodes, each with an *a priori* uncertainty of  $\pm 2$  km, were employed in the inversion, which after just two iterations had reduced the average absolute traveltimes residual from 0.28 s to 0.11 s, with no further significant improvement being evident (Tables 2 and 3). The ray diagram illustrates which portions

**Table 1.** Number of traveltimes picked for each phase from each shot in the WRR experiment.

Shot	1	2	3	31	4	41	5	51	6	7	8	9	10	Total
Phase														
<i>Pg</i>	94	3	88	194	82	59	176	109	134	186	14	34	158	1331
<i>PiP</i>	20			7						7		69		103
<i>PmP</i>	42		23	8			5			6		122	92	298
<i>Pi2P</i>			4	7			4					7		22

**Table 2.** Input parameters for the inversion and the resolution (R) and standard errors after Zelt & Smith (1992) for the various nodes for the final iteration of the WRR model.

Parameter type	No. of nodes	R	Std. error (km s <sup>-1</sup> or km)	Node coordinates (km)
Top layer	2	0.998	0.02	0, 20, 40, 60, 70, 80, 90, 100, 110, 120, 130, 140, 150, 155, 160, 165, 170, 175
Velocity		0.998	0.02	190, 200, 210, 220, 240, 260, 280, 300
2nd layer	2	0.997	0.03	0, 20, 40, 60, 80, 90, 100, 110, 120, 130, 140, 150, 160, 165
Velocity		0.998	0.02	170, 180, 190, 200, 210, 220, 230, 240, 250, 260, 270, 280, 300
3rd layer	2	0.9998	0.01	0, 20, 40, 60, 80, 100, 120, 140, 160
Velocity		0.9999	0.01	175, 195, 215, 235, 255, 275, 300
1st interface	5	0.999	0.1	0, 10, 20, 40, 60, 70, 80, 90
		0.998	0.1	100, 110, 120, 130, 140
		0.9995	0.1	150, 160, 170
		0.998	0.1	195, 205, 215, 225
		0.998	0.1	235, 255, 275, 300
2nd interface	6	0.997	0.2	0, 10, 20, 40, 60
		0.998	0.1	80, 100, 110
		0.999	0.1	120, 130, 140
		0.998	0.1	150, 160
		0.9997	0.1	175, 185, 195
		0.999	0.1	205, 215, 235, 255, 275, 300
<i>PiP</i> interface	3	0.92	0.6	0, 50, 100, 130
		0.88	0.7	150, 170
		0.99	0.2	190, 210, 230, 250, 300
<i>PmP</i> interface	6	0.76	1.0	0, 50, 70, 90, 110
		0.77	1.0	130
		0.17	1.8	150
		0.53	1.4	170
		0.53	1.4	190
		0.96	0.4	210, 230, 250, 270, 300
<i>Pi2P</i> interface	1	0.996	0.3	0, 50, 70, 90, 110, 130, 150, 170, 190, 210, 230, 250, 270, 300

of the interface are constrained (Fig. 10b). The three nodes are, however, all well resolved (Table 2) and all off-diagonal elements of the resolution matrix are small compared to the diagonal elements. Following the final inversion step, the boundary was made to shallow towards the coast outside the region of ray coverage for the model, in accordance with the results from previous experiments (Makris *et al.* 1983). Hence the boundary deepens slightly from 18–19 km below the coast at the NW end of the profile to 19–21 km depth beneath the whole profile east of profile km 80 (Fig. 11a).

### Step 3: lower crust and Moho

In attempting to invert the 298 traveltimes readings for the *PmP* phase for both the velocity of the lower crust and Moho depths, it was recognized at an early stage that there is a trade-off between the average velocity of the lower crust and the average structure of the Moho beneath the profile. It was thus decided to fix the velocity of the lower crust and invert the *PmP* arrivals for Moho structure only. An average value of 6.7 km s<sup>-1</sup> was chosen for the lower crustal veloc-

**Table 3.** Input parameters and results of the inversion of the WRR model.  $\sigma_d$  is the standard deviation of the traveltimes readings,  $\sigma_m$  is the *a priori* uncertainty in the model parameters and D is the overall damping factor (see, for example, Zelt & Smith 1992).

Phase	<i>Pg</i>	<i>PiP</i>	<i>PmP</i>	<i>Pi2P</i>
Parameter				
Ave. $\delta t$ start model (s)	0.17	0.28	0.21	0.16
Ave. $\delta t$ final model (s)	0.12	0.11	0.16	0.14
$\sigma_d$ (s)	0.10	0.20	0.20	0.20
$\sigma_m$ -interface (km)	3.0	2.0	2.0	5.0
$\sigma_m$ -velocity (km s <sup>-1</sup> )	0.5			
D	1.0	1.0	20.0	1.0

ity. This value is consistent with the 1-D modelling and results from previous experiments in the area (Ginzburg *et al.* 1979a,b; El-Isa *et al.* 1987) and has an error of  $\pm 0.2$  km s<sup>-1</sup>. However, values larger than 6.7 km s<sup>-1</sup> would increase the Moho depths to values which would exacerbate some of the discrepancies between the model derived in this study and models derived from previous experiments in

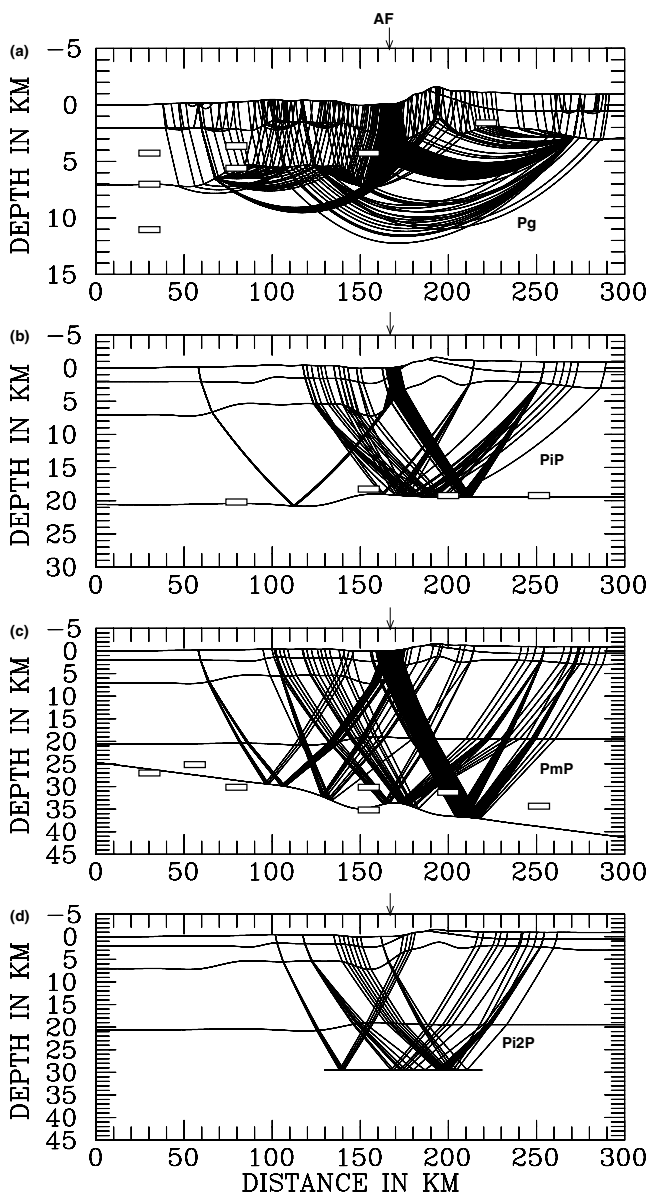


**Figure 10.** Ray diagrams for the final iterations of (a) the *Pg* phase, (b) the *PiP* phase, (c) the *PmP* phase and (d) the possible *Pi2P* phase. The bars represent the depth values for the respective interfaces (top of seismic basement, top of lower crust and Moho) from previous experiments in the area. Key: AF—Arava Fault.

the area (Ginzburg *et al.* 1979a,b; El-Isa *et al.* 1987). Having found a suitable average lower crustal velocity, it was then necessary to find an acceptable starting model for the Moho topography. Eventually a model with a dip down to the SE of  $2.9^\circ$  (uniform slope of 1 km in depth per 20 km in horizontal distance) was chosen, in preference to models with other smaller or greater uniform southeastward dips or a model with a horizontal Moho. In the first iteration of the inversion the interface was constrained to move by a constant amount in depth, in order to find the best depths for the preferred slope. This resulted in a decrease of the average absolute traveltimes difference from 0.21 s to 0.19 s. In the subsequent two iterations in which six independent interface nodes, each with an *a priori* uncertainty of  $\pm 2.0$  km, were employed, the average absolute traveltimes residual was reduced to 0.16 s (Tables 2 and 3), with no further significant improvement be-

ing evident. A major reason for utilizing six independent interface nodes was to answer the question of what the maximum amount of topography on the Moho under the Arava Valley might be. Of the six nodes, it can be seen that the node at 150 km is not well resolved in comparison to the other five nodes (Table 2). This is reflected in the ray diagram which shows that those interface nodes which are best resolved correlate with those parts of the interface that are hit by the largest number of rays (Fig. 10c). It should be mentioned though that in the first of the two iterations with six independent interface nodes, the node at 150 km was better resolved with a value of 0.48. Further, in both of the iterations with six independent interface nodes, the node at 150 km moved down and the node at 170 km moved up.

The Moho shows a steady increase in depth from about 26 km at the Mediterranean to about 39 km under the Jordan highlands (Fig. 11a). To the NW of the region of ray coverage for the model the Moho depth at the coast is in agreement with the value determined by Makris *et al.* (1983). To the SE of the region of ray coverage for the model the Moho has been continued to dip to the SE as also indicated by El-Isa *et al.* (1987), although the Moho depths in El-Isa *et al.* (1987) are a few kilometres less than those shown here. The fact that, during the inversion, the node at 150 km moved down and the node at 170 km moved up has resulted in a small but visible, asymmetric Moho topography of about 1.5 km under the Arava Valley. Other models with five or six independent interface nodes for the Moho were also tested. For example, moving the nodes by 10 km to the SE resulted in a similar shape for the Moho topography but with the topography variations shifted by 10 km to the SE. Combining the nodes at 130 and 150 km or the nodes at 170 and 190 km and inverting for just five independent interface nodes also resulted in similar topography variations for the Moho as those shown here. Only by combining the nodes at 150 and 170 km and inverting for five independent interface nodes produced a different result in which the Moho moved up to the NW of the node at 150 km and otherwise moved down. For other values for the average velocity of the lower crust a similar shape for the Moho topography to that shown here was also obtained. For higher values the difference in Moho depths between the nodes at 150 and 170 km decreased as the average velocity increased, while for an average velocity of  $6.6 \text{ km s}^{-1}$  the difference in Moho depths between the nodes at 150 and 170 km was greater than that shown here (Fig. 11a). From these model tests, it is thought that the small but visible, asymmetric Moho topography under the AF may, in fact, be real as most of the tested models seem to indicate the presence of such a structure. These results are also in good agreement with the NVR results (Figs 11b and A5).

*Pn* was not observed in the data from the WRR profile, probably due to a lack of energy from the borehole shots and quarry blasts beyond 150–170 km distance. A velocity of  $7.9 \text{ km s}^{-1}$  was assigned to the uppermost mantle based on previous experiments in which the *Pn* phase was observed almost exclusively from water shots and the *Pn* velocity ranged from  $7.8$ – $8.0 \text{ km s}^{-1}$  (Ginzburg *et al.* 1979a; El-Isa *et al.* 1987). From previous experiments in the area, El-Isa *et al.* (1987) found a crust-mantle transition zone with a thickness of about 4.5 km for the area east of the Arava Valley while Ginzburg *et al.* (1979b) found a crust-mantle transition zone of about 8 km thickness within the Arava Valley. In contrast, Ginzburg *et al.* (1979a) modelled the Moho as a first order discontinuity both to the west of the Arava Valley as well as within the Arava Valley. These previous experiments were carried out with station spacings typically on the order of about 5 km, which is significantly sparser than the station spacing of the WRR profile. On the WRR profile

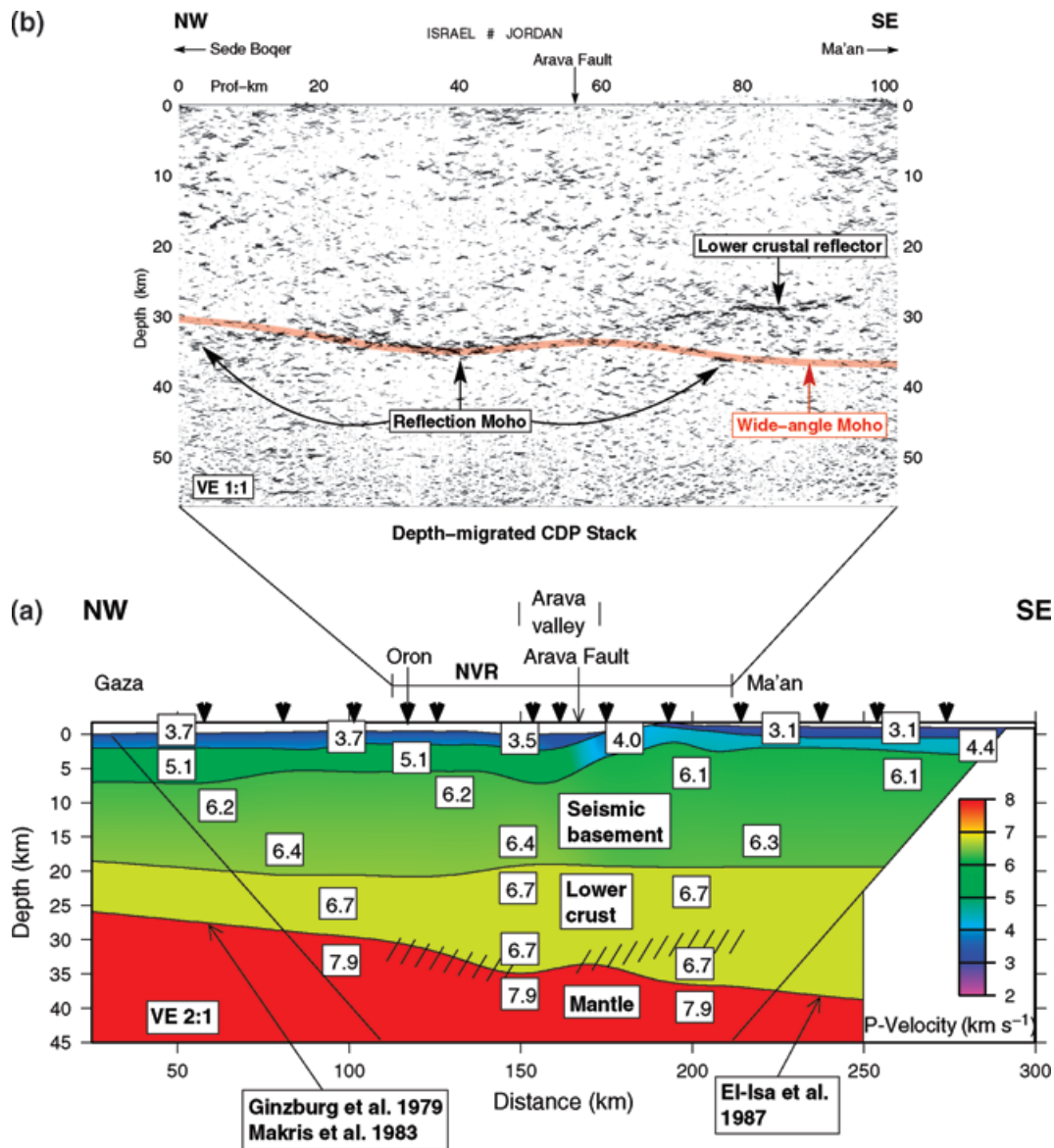


**Figure 11.** (a) 2-D P-velocity model (velocities in  $\text{km s}^{-1}$ ) for the WRR experiment. The shots (triangles at top) were recorded by 99 three-component instruments along the whole profile and 125 vertical component geophone groups in the Arava Valley (see also Fig. 2a). For accuracy estimates of velocities and interface depths see text. Only the central area inside the diagonal lines is resolved in this study. Outside this area the model is based on previous work (Fig. 1b; Ginzburg *et al.* 1979a; Ginzburg *et al.* 1979b; Makris *et al.* 1983; El-Isa *et al.* 1987). The hatched symbols near the Moho, the border between yellow and red colours, indicate the location of bands of strong reflections in the NVR migrated section (b). Note vertical exaggeration of 2:1. (b) Automatic line drawing of the depth-migrated seismic CDP section of the NVR experiment (Fig. A5). The red band indicates the location of the Moho (crust/mantle boundary) as derived from the WRR experiment in (a). The black arrows mark the break-off of reflectivity, generally interpreted as the Moho in seismic reflection data.

strong reflections from the Moho have been observed in the densely spaced data from the Arava Valley from shots 3, 9 and 10 (Figs 4b, 8b and 9b). These reflections are from around the critical region and, in fact, some are slightly under-critical according to the model shown here (Fig. 11a) in which the Moho is modelled as a first order discontinuity. The synthetic seismogram section for shot 9 (Fig. 12) shows that the Moho reflection,  $PmP$ , has significant energy with respect to the other phases,  $Pg$  and  $PiP$ , at under-critical distances of 80–90 km in agreement with the observed data (Fig. 8b). Thus it is thought that there is probably no crust-mantle transition zone along the WRR profile either east or west of the Arava Valley. As the WRR profile crosses the Arava Valley at a point where the Valley is only

about 20 km wide, the profile is probably not optimally positioned to answer the question of whether or not a crust-mantle transition zone extends in the N–S direction beneath the Arava Valley itself.

Finally, in this section the inversion of the 22 arrivals from the possible additional intra-crustal reflection,  $Pi2P$ , will be described. The 2-D starting model consisted of a horizontal interface at about 30 km depth. With only one independent interface node, one iteration was enough to determine the average depth for the boundary associated with this possible reflection (Tables 2 and 3). It turns out that this possible reflector is at an average depth of about 30 km and the ray diagram shows that it might exist between model km 130 and 220 (Fig. 10d).

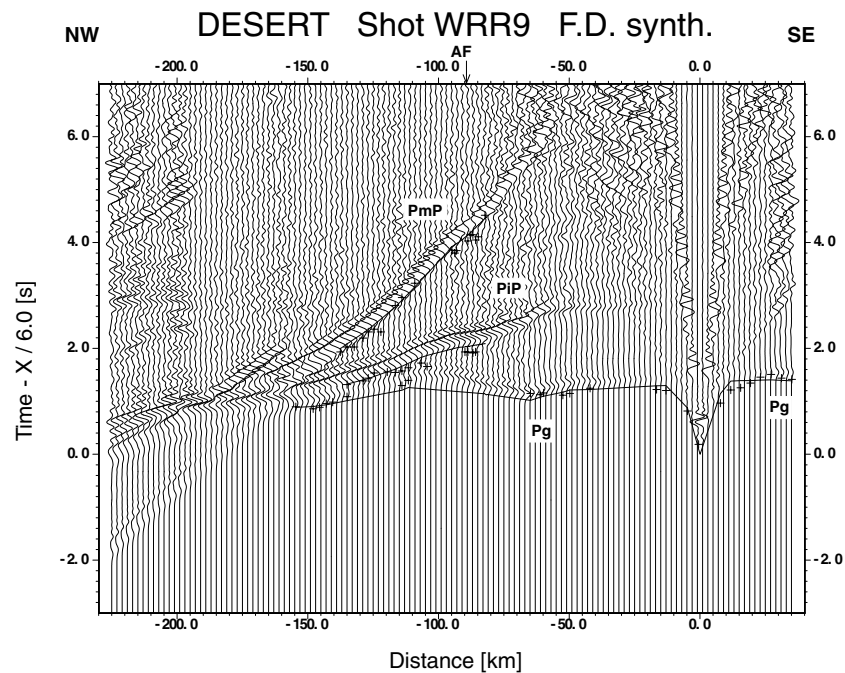


**Figure 12.** Synthetic seismogram section, calculated with the finite-difference method, for shot 9 along WRR profile. The record section reduced with a velocity of  $6 \text{ km s}^{-1}$  shows the vertical component of  $P$ -wave motion in which each trace is normalized individually. Continuous lines represent phases calculated from the model shown in Fig. 11(a), while crosses represent traveltimes from the observed data in Fig. 8(a). Key: see Fig. 3.

#### 4 DISCUSSION

In the following we will try to answer the four central questions raised in the introduction.

##### (1) What is the crustal structure at the DST in the Arava Valley?

In deep crustal reflection data the Moho is commonly defined as the break-off of lower crustal reflectivity (Fig. 11b). The increase in Moho depth from  $\sim 30$  to  $38 \text{ km}$ , that is observed in the WRR data beneath the NVR profile, is more or less in accordance with the NVR data. A few small discrepancies between the reflection and refraction seismic data (as for example at the western end of the NVR line) are not unusual for coincident seismic reflection/refraction surveys (see e.g. Mooney & Brocher 1987). Note also that reflections from Moho depths typically have dominant frequencies of  $12\text{--}13 \text{ Hz}$  in the NVR data, in contrast to  $6\text{--}7 \text{ Hz}$  in the WRR data. At the same time the differences between the reflection and refraction Moho are in the range of measurement uncertainties (see also WRR modelling, Section 3.3).

In comparing the depths to the seismic basement with those obtained from previous experiments in the area, the depths obtained in this study west of the Arava Valley (Figs 10a and 11a) are smaller than those obtained by Ginzburg *et al.* (1979a). This may be due in part to somewhat lower average velocities used by Ginzburg *et al.* (1979a). On the other hand the depths to the seismic basement obtained here west of the Arava Valley are in good agreement with those obtained by Perathoner (1979). The larger value for the depth to the seismic basement beneath the coast obtained by Makris *et al.* (1983) from the offshore-onshore experiment in 1978 probably indicates that the depth to the seismic basement increases towards the coast to the NW of the region of ray coverage for the model obtained here. Beneath the Arava Valley itself, the depth to the seismic base-

ment obtained here is greater than those obtained by Ginzburg *et al.* (1979a) and Perathoner (1979) from the N–S profile within the Arava Valley (Fig. 1b). This is probably due to the fact that although, for the N–S profile, the shot was in the Dead Sea, the recording stations were at the western side of the Arava Valley and sometimes on the shoulders of the Arava Valley. To the east of the Arava Valley the depth to the seismic basement obtained here is within  $1 \text{ km}$  of the depth obtained by El-Isa *et al.* (1987) from the N–S profile on the eastern shoulder of the Arava Valley (Fig. 1b). The depths to the boundary between the upper and lower crust obtained in this study (Figs 10b and 11a) agree to within  $1 \text{ km}$  with the depths to this boundary obtained from the previous experiments in this area (Fig. 1b; Ginzburg *et al.* 1979a; El-Isa *et al.* 1987).

With respect to the depths to the Moho, west of the Arava Valley there is agreement to within  $3 \text{ km}$  between the depths obtained here (Fig. 10c) and those obtained by Ginzburg *et al.* (1979a) and Makris *et al.* (1983). Beneath the Arava Valley itself the Moho depth obtained here agrees with that obtained by Perathoner (1979) from the N–S profile within the Arava Valley, but it is  $5 \text{ km}$  deeper than the value obtained by Ginzburg *et al.* (1979a). To the east of the Arava Valley the Moho depths obtained here are also about  $5 \text{ km}$  deeper than those obtained by El-Isa *et al.* (1987) from the N–S profiles on the eastern shoulder of the Arava Valley. In fact, the Moho depths obtained by El-Isa *et al.* (1987) from the N–S profiles on the eastern shoulder of the Arava Valley (Fig. 10c) are more in agreement with the depth at which strong reflections are observed in the NVR section (Fig. 11b). In order to find out where  $PmP$  reflections would occur in the record sections assuming that the Moho depths are as indicated by either the near-vertical incidence reflection section or by El-Isa *et al.* (1987), a model was constructed with Moho depths taken from the near-vertical incidence reflection section and El-Isa *et al.* (1987) and an average lower crustal velocity of  $6.7 \text{ km s}^{-1}$ . Tracing rays through this model results in arrival times

for the *PmP* reflection which are 0.8–1.0 s earlier than those for the preferred model shown here (Fig. 11a) in the record sections from the densely spaced data from the Arava Valley from shots 9 and 10 (Figs 8b and 9b). In these data there are no strong reflections 0.8–1.0 s earlier than the *PmP* reflections shown. For this reason and as the data from the previous experiments in the area are sparser than the data along the WRR profile, it is thought that the Moho depths obtained here are more accurate than those obtained by El-Isa *et al.* (1987). Alternatively, the discrepancy may be, at least in part, due to strong 3-D variations of the Moho in the vicinity of the DESERT profile. Such variations are evident in the receiver-function data (A. Mohsend, personal communication, 2003).

A remarkable feature in Fig. 11(b) is a zone of high reflectivity at a depth of 28 km below the Jordan highlands between profile km 78 and 92. This is about the depth and position along the profile from which the possible phase, *Pi2P* in the WRR data is reflected, although the boundary associated with the *Pi2P* phase, if present, would have to occur for at least about 90 km under the profile (Fig. 10d) instead of just about 20 km as identified in the NVR data. This zone of high reflectivity in the NVR data might be due to a lithological contrast caused by underplating. In this case higher velocities of about  $7.0 \text{ km s}^{-1}$  would be expected to occur across the region of high reflectivity. If a  $7.0 \text{ km s}^{-1}$  layer of limited thickness is, in fact, present at about 30 km depth, this would only have a small effect on the estimated Moho depths, such that they would still be within the error limits of  $\pm 3 \text{ km}$  given above (Section 3.3). Strong magmatic activity that occurred in the region both in Late Precambrian/Early Cambrian, Cretaceous and Neogene times could possibly have caused such a proposed underplating, or sill-like intrusions into the lower crust. Another possibility for the creation of such a high reflectivity is a zone of localized strain close to the base of the crust, which is in agreement with the conclusions of Sobolev (unpublished data) (see also later discussion) which show a zone of high shear deformation and possible lower crustal flow east of the transform. It is expected that a gravity analysis currently being carried out along the profile might give some further constraints for interpreting these reflectors. The high reflectivity at Moho depth west of the AF is in accordance with the eastern part of a deep seismic reflection line between the Mediterranean and the Dead Sea (Yuval & Rotstein 1987; Rotstein *et al.* 1987) that shows a similar reflectivity pattern of the crust as observed here.

### (2) Does the DST cut through the whole crust?—Yes

Imaging near-vertical structures by near-vertical seismic reflection techniques is difficult (e.g. Meissner 1996). It is, however, possible to get indirect evidence of the depth continuation of steeply dipping faults by the offset of crustal reflectors or an observed change in crustal reflectivity.

However, although the DST/AF is clearly recognized on satellite data as a rather straight line between the Red Sea and the Dead Sea (DESERT Team 2000) it cannot unambiguously be delineated in the Common Depth Point (CDP) section (Figs 11b and A5). There is no pronounced difference in crustal structure west and east of the Arava Fault and in the immediate vicinity of its surface trace sedimentary reflections are missing. The absence of sedimentary reflectors might be due to strong deformation of the rocks close to the fault, but could also be caused by the absorption of high frequencies (Fig. A2) in an area covered by sand dunes and alluvium.

Whereas a possible Moho offset has been proposed for the San Andreas Fault in northern California from deep crustal seismic re-

lection and refraction studies (Henstock *et al.* 1997), and for the DST north of the Dead Sea Basin from the analysis of gravity data (Ten Brink *et al.* 1990), there is no evidence for such an offset at the AF along the NVR profile. Nonetheless it is inferred that the AF reaches down to the mantle, changing into a broader deformation zone at mid-crustal level, because of the following reasons:

(1) At Moho depth an  $\sim 15 \text{ km}$  wide zone (profile km 54 to 70 in Figs 11b and A5) beneath the surface trace of the AF is observed that lacks the strong reflectors observed farther to the west and the lower crustal reflectors observed to the east. From this it is derived that the fault zone becomes broader in the lower crust. The strong reflections beneath the AF at about 18 km depth are thought to occur at the upper/lower crust boundary and are linked to a velocity jump from  $6.4$  to  $6.7 \text{ km s}^{-1}$  (Fig. 11a). There is no good expression of this boundary elsewhere in the NVR data. This is taken as an indication for a zone of localized shear strain between the felsic upper and mafic lower crust related to the transform motion along the AF. Whereas Furlong *et al.* (1989) and Brocher *et al.* (1994) interpreted a similar subhorizontal surface at 15–20 km depth below the San Andreas Fault Zone in the San Francisco Bay area as a possible detachment zone of the San Andreas Fault, linking it to the Hayward/Calaveras fault system, Holbrook *et al.* (1996) interpreted it as corresponding to the top of the lower crust, acting as a whole to accommodate shear deformation in a broad zone. Here we propose a similar model for the DST as Holbrook *et al.* (1996).

(2) The small but visible, asymmetric topography of the Moho below the Arava Valley in the WRR model (profile km 130 to 170 in Fig. 11a) is also consistent with the NVR data. This is another piece of evidence for the AF cutting through the whole crust. Whereas a bending down of the Moho, or a ‘Moho keel’ has been put forward for some Paleozoic strike-slip regions in transpressional tectonic regimes (McBride 1994; Stern & McBride 1998), this coupled upward-downward structure of the Moho might be due to the transtensional character of the DST between the Red Sea and the Dead Sea (see also later discussion).

(3) Reflectors in the lowermost crust (25–32 km depth from profile km 55 to 70 in Fig. 11b) that dip away from the suspected fault zone and that are most pronounced east of the AF, might correspond to anisotropic fabrics developing along mylonitic shear zones, similar to the dipping reflectors beneath the Walls Boundary strike-slip fault in the northern British Caledonides (McBride 1994).

Our conclusion from these seismic data, namely that the AF reaches down to the mantle and changes into a broader deformation zone at mid-crustal level, agrees also with the results of the thermo-mechanical modelling of the DST (Sobolev, unpublished data). These results show that shear-deformation focuses in one or two major faults in a 20–40 km wide region in the upper crust with minimal strength, and that a broad mechanically weak decoupling zone extends vertically from the lower crust into the asthenosphere. Further evidence for such an extension of this decoupling zone in the asthenosphere comes from teleseismic SKS-splitting observations along the NVR profile (Rümpker *et al.* 2003). This deep reaching boundary layer is thought to accommodate the transform motion between the African and the Arabian plates (Fig. 1).

### (3) Does rifting/extension play an important role in the dynamics of the DST?—No.

Some features in the near-surface structure of the Arava Valley, e.g. surface topographic expression, sedimentary fill and normal faults

at the edge of the valley, resemble those of rift structures. However, the narrow, only  $\sim 10$  km wide, shallow sedimentary basin mainly to the west of the AF (Fig. 2b), a seismic basement offset of 3 to 5 km on the eastern side of the Arava Valley and the small but visible, asymmetric Moho topography ( $\sim 1.5$  km) with a coupled upward-downwarp structure beneath the Arava Valley (Fig. 11), although possibly related to the slight extension across this part of the DST, are untypical for rift structures. For example, the southern portion of the Kenya rift, a classical continental rift, has been under extension since about 10 Ma, and the Moho there is uplifted 5–10 km causing considerable crustal thinning (Mechie *et al.* 1997). We therefore conclude that rifting-type deformation (fault perpendicular extension) did not play a dominant role in shaping the crustal structure of the DST. A thermo-mechanical model of the DST by Sobolev (unpublished data) confirms this by showing that the crustal structure of the DST results mainly from the geologically documented 105 km left-lateral displacement between the Arabian plate and the African plate (Figs 13a and b) placing lithospheric blocks with different crustal structures opposite each other. The modelling also supports the scenario that changes in surface and Moho topography and in crustal structure result from large, localized deformation accommodating the transform motion within a narrow zone crossing the entire crust. However, this process is combined with less than 4 km of fault-perpendicular extension (Garfunkel 1981; Sobolev *et al.* 2003 Fig. 13c). Thus the ‘rift component’ at the DST between the Dead Sea and the Gulf of Aqaba, defined as the ratio between fault perpendicular extension [4 km] and strike slip motion [105 km], is probably smaller than 4 per cent. This small extension nevertheless produces a large topography because the extension is localized within the narrow (20 km wide) upper mantle and lower crustal shear zones, where viscosity is reduced due to the high strain rate produced by the strike-slip motion (Sobolev *et al.* 2003), thus giving the Arava Valley the appearance of a rift valley.

(4) *Are there structural similarities between the DST and the SAF system despite their different geological history and setting?—Yes and No.*

A comparison with the San Andreas Fault (SAF), another end-member of transform structures (see e.g. Holbrook *et al.* 1996; Bonner & Blackwell 1998), shows several differences, especially in the shallow structure, and some similarities in the deeper structure. Fault Zone Guided Waves from controlled source experiments in the Arava Valley (Haberland *et al.* 2003) sample the top few hundred meters of the Arava Fault and are best explained by a fault model with a narrow, only 3–10 m wide low-velocity zone. This thickness is much smaller than the typical width of 100 to 170 m of low-velocity zones in the SAF system (Li *et al.* 1990), and is possibly due to the smaller total slip on the DST (105 km) versus the slip of more than 350 km at the SAF, or it could be a local feature controlled by the young sediments in the area where the DESERT profile crosses the AF. In contrast to the SAF the Arava Fault under the DESERT profile acts as a localized fluid barrier separating a high- from a low-velocity block in the uppermost crust. This contrast is visible in the combined magnetotelluric sounding and high-resolution tomography of Ritter *et al.* (2003). Such a feature is remarkably different from active segments of the SAF, which typically show a conductive fault core acting as a fluid conduit (Unsworth *et al.* 2000).

If, however, deeper crustal and mantle structures are compared, it becomes apparent that both transform systems show deep reaching deformation zones (Sobolev, unpublished data, Rumpker *et al.* 2003 for the DST and Holbrook *et al.* 1996; Henstock *et al.*

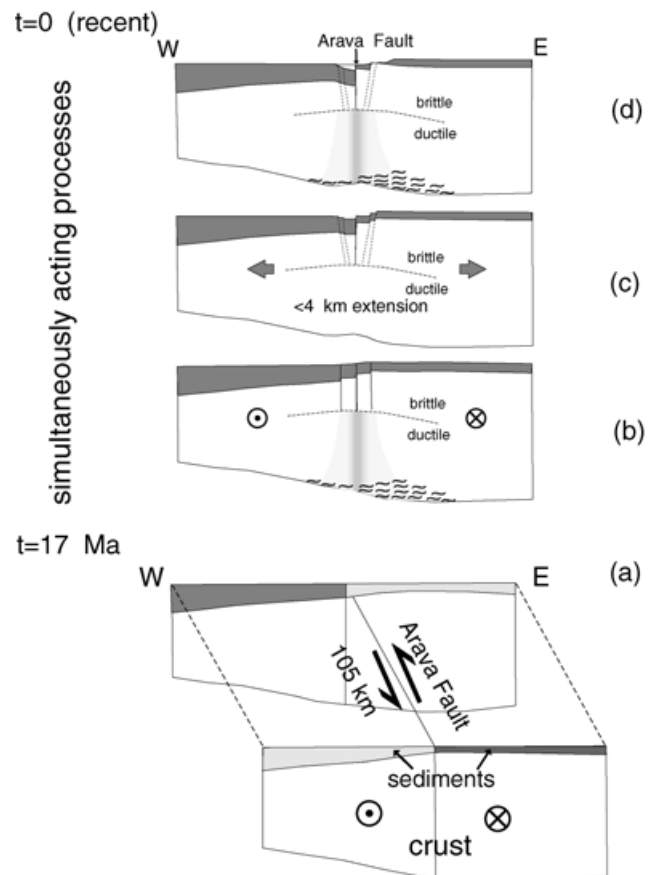


**Figure 13.** Sketch of the DST dynamics along the DESERT profile, based on results shown in Fig. 11 and the results of Sobolev (unpublished data). (a) Crustal structure before the beginning of transform motion, i.e. 17 Ma ago. The Phanerozoic sedimentary cover is shaded, dark shading indicates sections which today are facing each other and were crossed by the DESERT profile. (b) Transform motion of  $\sim 105$  km results in a crustal cross-section with a significantly different structure east and west of the Arava Fault. The shaded domain shows the region of ductile shear deformation (Sobolev, unpublished data). Wavelike symbols indicate lower crustal regions of high reflectivity (Fig. 11) possibly related to lower crustal flow. (c) Associated minor tension ( $\sim 4$  km) produces subsidence and flexure in the western block accommodated by uplift of the eastern block, with a similar small amplitude flexure at the Moho (Fig. 11). (d) Erosion and sedimentation produces the present day structure.

1997; Unsworth *et al.* 1997; Silver 1996 for the SAF) accompanied by a strong asymmetry in subhorizontal lower crustal reflectors (lower crustal flow, sill-like intrusions?). We therefore suggest that these features are common features of continental transform plate boundaries.

## 5 CONCLUSIONS

Our study provides the first whole-crustal image across the Dead Sea Transform (DST), one of the Earth's major transform faults. Under the Arava Fault (Fig. 11), the main fault of the southern DST system, the seismic basement is offset by several kilometres, but the Moho depth increases steadily from  $\sim 26$  km at the Mediterranean to  $\sim 39$  km under the Jordan highlands, except for a small but visible, asymmetric topography under the Arava Valley. The general trend of continuous Moho-depth increase is confirmed by the interpretation of potential field data (Al-Zoubi & Ben-Avraham 2002) and the results of a receiver functions study (A. Mohsen, personal

communication, 2003). Based on the interpretation of the NVR data, we infer that the AF cuts through the crust, becoming a broad zone in the lower crust, and reaches down to the mantle. This agrees with the results of the thermo-mechanical modelling of Sobolev *et al.* (2003) and the SKS-splitting observations by Rumpker *et al.* (2003), which suggest that the DST cuts through the whole lithosphere, thus accommodating the motion between the African and the Arabian plates (Fig. 1). The lack of significant uplift of the Moho under the Arava Valley speaks strongly against a potential rift structure in this area. We therefore conclude that rift-type deformation (fault perpendicular extension) did not play a dominant role in the dynamics of the DST, a fact corroborated again by the results of Sobolev (unpublished data). Although the shallow structure at the DST differs significantly from the structure at the San Andreas Fault, the deep reaching deformation zones accompanied by a strong asymmetry in subhorizontal lower crustal reflectors appear to be similar for both fault zone systems. We therefore suggest that these deep features are common for large continental transform plate boundaries.

## ACKNOWLEDGMENTS

We thank U. ten Brink, J. Hole, M. Zoback, C. Prodehl and three anonymous reviewers for comments on an earlier version of this manuscript. We thank the National Ministry of Infrastructure of Israel, the Natural Resources Authority of Jordan and the An-Najah National University in Nablus, Palestine, for their support. We thank our contractors the Geophysical Institute of Israel, the Site Group (Jordan) and the Chemical and Mining Industries (Jordan) for their excellent work under difficult logistic conditions, and the Oron mine (Israel) and the Eshidiyah mine (Jordan) for their cooperation. The instruments were provided by the Geophysical Instrument Pool of the GeoForschungsZentrum Potsdam (GFZ). The experiments were funded by the Deutsche Forschungsgemeinschaft, the GFZ and the Minerva Dead Sea Research Centre.

## REFERENCES

- Al-Zoubi, A. & Ben-Avraham, Z., 2002. Structure of the Earth's crust in Jordan from potential field data, *Tectonophysics*, **346**, 45–59.
- Amiran, D.H.K., Ariei, E. & Turcotte, T., 1994. Earthquakes in Israel and Adjacent Areas: Macroseismic Observations since 100 B.C.E., *Israel Exploration Journal*, **44**, 260–305.
- Bartov, Y., Avni, Y., Calvo, R. & Frieslander, U., 1998. The Zofar Fault—A major intra-rift feature in the Arava rift valley, *Geological Society of Israel, Current Research*, **11**, 27–32.
- Ben-Avraham, Z., Ginzburg, A., Makris, J. & Eppelbaum, L., 2002. Crustal structure of the Levant Basin, eastern Mediterranean, *Tectonophysics*, **346**, 23–43.
- Bonner, J.L. & Blackwell, D.D., 1998. Temperatures and earthquakes in California, in *Proceed. Int. Conf. 'The Earths thermal field and related research methods'*, Moscow, May 19–21, 1998, pp. 41–46, Moscow State Geological Prospecting Academy, Moscow.
- Birt, C.S., Maguire, P.K.H., Khan, M.A., Thybo, H., Keller, G.R. & Patel, J., 1997. The influence of pre-existing structures on the evolution of the southern Kenya Rift Valley—evidence from seismic and gravity studies, *Tectonophysics*, **278**, 211–242.
- Braile, L.W., Wang, B., Daudt, C.R., Keller, G.R. & Patel, J.P., 1994. Modelling the 2-D seismic velocity structure across the Kenya rift, *Tectonophysics*, **236**, 251–269.
- Brocher, T.M., McCarthy, J., Hart, P.E., Holbrook, W.S., Furlong, K.P., McEvelly, T.V., Hole, J.A. & Klempner, S.L., 1994. Seismic evidence for a lower-crustal detachment beneath San Francisco Bay, California, *Science*, **265**, 1436–1439.
- Cervený, V., Molotkov, I.A. & Psencik, I., 1977. *Ray Method in Seismology*, University of Karlova, Prague.
- DESERT Team, 2000. Multinational geoscientific research effort kicks off in the Middle East, *EOS, Trans. Am. geophys. Un.*, **81**, 609, 616–617.
- El-Isa, Z., Mechie, J., Prodehl, C., Makris, J. & Rihm, R., 1987. A crustal structure study of Jordan derived from seismic refraction data, *Tectonophysics*, **138**, 235–253.
- Freund, R., Garfunkel, Z., Zak, I., Goldberg, M., Weissbrod, T. & Derin, B., 1970. The shear along the Dead Sea rift, *Phil. Trans. R. Soc. Lond.*, **A**, **267**, 107–130.
- Frieslander, U., 2000. The structure of the Dead Sea Transform emphasizing the Arava, using new geophysical data, PhD thesis, Hebrew University, Jerusalem (in Hebrew).
- Fuchs, K. & Müller, G., 1971. Computation of synthetic seismograms with the reflectivity method and comparison with observations, *Geophys. J. R. astr. Soc.*, **23**, 417–433.
- Fuis, G.S., Ryberg, T., Godfrey, N., Okaya, D.A. & Murphy, J.M., 2001. Crustal structure and tectonics from the Los Angeles basin to the Mojave Desert, southern CA, *Geology*, **29**, 15–18.
- Furlong, K.P., Hugo, W.D. & Zandt, G., 1989. Geometry and evolution of the San Andreas fault zone in southern California, *J. geophys. Res.*, **94**, 3100–3110.
- Garfunkel, Z., 1981. Internal structure of the Dead Sea leaky transform (rift) in relation to plate kinematics, *Tectonophysics*, **80**, 81–108.
- Garfunkel, Z. & Derin, B., 1984. Permian–early Mesozoic tectonism and continental margin formation in Israel and its implications for the history of the Eastern Mediterranean, in *The Geologic Evolution of the Eastern Mediterranean*, pp. 187–201, eds Dixon, J.E. & Robertson, A.H.F. *Geol. Soc. Spec. Pub.*, No. 17, London, UK.
- Garfunkel, Z., Zak, I. & Freund, R., 1981. Active faulting in the Dead Sea Rift, *Tectonophysics*, **80**, 1–26.
- Ginzburg, A., Makris, J., Fuchs, K., Prodehl, C., Kaminski, W. & Amitai, U., 1979a. A seismic study of the crust and upper mantle of the Jordan-Dead Sea Rift and their transition toward the Mediterranean Sea, *J. geophys. Res.*, **84**, 1569–1582.
- Ginzburg, A., Makris, J., Fuchs, K., Perathoner, B. & Prodehl, C., 1979b. Detailed structure of the crust and upper mantle along the Jordan-Dead Sea Rift, *J. geophys. Res.*, **84**, 5605–5612.
- Haberland, Ch. *et al.*, 2003. Modeling of seismic guided waves at the Dead Sea Transform, *J. geophys. Res.*, **108**, no. B7, 2342, doi: 10.1029/2002JB002309.
- Henjes-Kunst, F., Altherr, R. & Baumann, A., 1990. Evolution and composition of the lithospheric mantle underneath the western Arabian Peninsula: constraints from Sr-Nd isotope systematics of mantle xenoliths, *Contrib. Mineral. Petrol.*, **105**, 460–472.
- Henstock, T.J., Levander, A. & Hole, J.A., 1997. Deformation in the Lower Crust of the San Andreas Fault System in Northern California, *Science*, **278**, 650–653.
- Hirsch, F. & Picard, L., 1988. The Jurassic facies in the Levant, *Journal of Petroleum Geology*, **11**, 277–307.
- Holbrook, W.S., Brocher, T.M., Ten Brink, U.S. & Hole, J.A., 1996. Crustal structure of a transform plate boundary: San Francisco Bay and the central California continental margin, *J. geophys. Res.*, **101**, 22 311–22 334.
- Hole, J.A., Catchings, R.D., St. Clair, K.C., Rymer, M.J., Okaya, D.A. & Carney, B.J., 2001. Steep-dip seismic imaging of the shallow San Andreas Fault near Parkfield, *Science*, **294**, 1513–1515.
- Ibrahim, K.M. & McCourt, W.J., 1995. Neoproterozoic granitic magmatism and tectonic evolution of the northern Arabian Shield: evidence from southwest Jordan, *Journal of African Earth Sciences*, **20**, 103–118.
- Kelly, K.R., Ward, R.W., Treitel, S. & Alford, R.M., 1976. Synthetic seismograms: a finite difference approach, *Geophysics*, **41**, 2–27.
- Ken-Tor, R., Agnon, A., Enzel, Y., Stein, M., Marco, S. & Negendank, J.F.W., 2001. High-resolution geological record of historic earthquakes in the Dead Sea basin, *J. geophys. Res.*, **106**, 2221–2234.
- Klinger, Y., Avouac, J.P., Dorbath, L., Abou Karaki, N. & Tisnerat, N., 2000. Seismic behaviour of the Dead Sea fault along Arava Valley, Jordan, *Geophys. J. Int.*, **142**, 769–782.

- Li, Y.-L., Leary, P., Aki, K. & Malin, P.E., 1990. Seismic trapped modes in the Oroville and San Andreas Fault zone, *Science*, **249**, 763–765.
- Lutter, W.J. & Nowack, R.L., 1990. Inversion for crustal structure using reflections from the PASSCAL Ouachita experiment, *J. geophys. Res.*, **95**, 4633–4646.
- Lutter, W.J., Nowack, R.L. & Braile, L.W., 1990. Seismic imaging of upper crustal structure using traveltimes from the PASSCAL Ouachita experiment, *J. geophys. Res.*, **95**, 4621–4631.
- Maguire, P.K.H., Swain, C.J., Masotti, R. & Khan, M.A., 1994. A crustal and uppermost mantle cross-sectional model of the Kenya Rift derived from seismic and gravity data, *Tectonophysics*, **236**, 217–249.
- Makris, J., Ben-Avraham, Z., Behle, A., Ginzburg, A., Giese, P., Steinmetz, L., Whitmarsch, R.B. & Eleftheriou, S., 1983. Seismic refraction profiles between Cyprus and Israel and their interpretation, *Geophys. J. R. astr. Soc.*, **75**, 575–591.
- McBride, J.H., 1994. Structure of a continental strike-slip fault from deep seismic reflection: Walls Boundary fault, northern British Caledonides, *J. geophys. Res.*, **99**, 23 985–24 005.
- Mechie, J. & Prodehl, C., 1988. Crustal and uppermost mantle structure beneath the Afro-Arabian rift system, *Tectonophysics*, **153**, 103–121.
- Mechie, J., Keller, G.R., Prodehl, C., Khan, M.A. & Gaciri, S.J., 1997. A model for the structure, composition and evolution of the Kenya rift, in *Structure and Dynamic Processes in the Lithosphere of the Afro-Arabian Rift System*, vol. 278, pp. 95–119, eds Fuchs, K., Altherr, R., Mueller, B. & Prodehl, C., Tectonophysics.
- Meissner, R., 1996. Faults and folds, fact and fiction, *Tectonophysics*, **264**, 279–293.
- Mooney, W.D. & Brocher, T.M., 1987. Coincident Seismic Reflection/Refraction Studies of the Continental Lithosphere: A Global Review, *Rev. Geophys.*, **25**, 723–742.
- Perathoner, B., 1979. Interpretation refraktionsseismischer Experimente in Israel im Bereich des Jordangrabens, Diploma thesis, Karlsruhe University, Karlsruhe.
- Prodehl, C., Fuchs, K. & Mechie, J., 1997. Seismic-refraction studies of the Afro-Arabian rift system—a brief review, in *Structure and Dynamic Processes in the Lithosphere of the Afro-Arabian Rift System*, eds Fuchs, K., Altherr, R., Mueller, B. & Prodehl, C., *Tectonophysics (Special Issue)*, **278**, 1–13.
- Podvin, P. & Lecomte, I., 1991. Finite difference computation of travel times in very contrasted velocity models: a massively parallel approach and its associated tools, *Geophys. J. Int.*, **105**, 271–284.
- Quennell, A.M., 1958. The structural and geomorphic evolution of the Dead Sea rift, *Quarterly Journal of the Geological Society of London*, **114**, 2–24.
- Reynolds, A.C., 1978. Boundary conditions for the numerical solution of wave propagation problems, *Geophysics*, **43**, 1099–1110.
- Ritter, O., Ryberg, T., Weckmann, U., Hoffmann-Rothe, A., Abueladas, A., Garfunkel, Z. & the DESERT Research Group, 2003. Geophysical images of the Dead Sea Transform in Jordan reveal an impermeable barrier for the fluid flow, *Geophys. Res. Lett.*, **30**, no. 14, 1741, doi: 10.1029/2003GL017541.
- Rotstein, Y., Yuval, Z. & Trachtman, P., 1987. Deep seismic reflection studies in Israel—an update, *Geophys. J. R. astr. Soc.*, **89**, 389–394.
- Rümpker, G., Ryberg, T., Bock, G. & DESERT Group, 2003. Boundary-layer mantle flow under the Dead Sea Transform fault from seismic anisotropy, *Nature*, **425**, 497–501.
- Ryberg, T. & Fuis, G.S., 1998. The San Gabriel Mountains bright reflective zone: possible evidence of mid-crustal thrust faulting in southern California, *Tectonophysics*, **286**, 31–46.
- Sandmeier, K.-J., 1990. Untersuchung der Ausbreitungseigenschaften seismischer Wellen in geschichteten und streuenden Medien, *PhD thesis*, Karlsruhe University, Karlsruhe.
- Schneider, W.A., Ranzinger, K.A., Balch, A.H. & Kruse, C., 1992. A dynamic programming approach to first arrival travel time computation in media with arbitrarily distributed velocities, *Geophysics*, **57**, 39–50.
- Sengör, A.M.C., 1979. The North Anatolian transform fault: its age, offset and tectonic significance, *J. geol. Soc. Lond.*, **136**, 269–282.
- Silver, P.G., 1996. Seismic anisotropy beneath the continents: Probing the depth of geology, *Ann. Rev. Earth Planet. Sci.*, **24**, 385–432.
- Sneh, A., Bartov, Y., Weissbrod, T. & Rosensaft, M., 1998. Geological Map of Israel 1:200,000, sheets 3 and 4: Geological Survey of Israel, Jerusalem.
- Stern, R.J., 1994. Arc Assembly and Continental Collision in the Neoproterozoic East African Orogen: Implications for the Consolidation of Gondwanaland, *Annu. Rev. Earth Planet. Sci.*, **22**, 319–351.
- Stern, T.A. & McBride, J.H., 1998. Seismic exploration of continental strike-slip zones, *Tectonophysics*, **286**, 63–78.
- Stoeser, D.B. & Camp, V.E., 1985. Pan-African microplate accretion of the Arabian Shield, *Geological Society of America Bulletin*, **96**, 817–826.
- Ten Brink, U.S., Schoenberg, N., Kovach, R.L. & Ben-Avraham, Z., 1990. Uplift and a possible Moho offset across the Dead Sea transform, *Tectonophysics*, **180**, 71–85.
- Unsworth, M.J., Malin, P.E., Egbert, G.D. & Booker, J.R., 1997. Internal structure of the San Andreas fault at Parkfield, California, *Geology*, **25**, 359–362.
- Unsworth, M.J., Bedrosian, P., Eisel, M., Egbert, G.D. & Siripunvaraporn, W., 2000. Along strike variations in the electrical structure of the San Andreas Fault at Parkfield, California, *Geophys. Res. Lett.*, **27**, 3021–3024.
- Vidale, J., 1988. Finite-difference calculation of travel times, *Bull. seism. Soc. Am.*, **78**, 2062–2076.
- Weissbrod, T., 1969. The Paleozoic of Israel and adjacent countries; Part 1: The subsurface Paleozoic stratigraphy of southern Israel, *Isr. Geol. Surv. Bull. Inst. Pet. Res. Geophys. Rep.*, **1008**, 1–23.
- Weissbrod, T. & Sneh, A., 2002. Sedimentology and Paleogeography of the Late Precambrian-Early Cambrian Arkosic and Conglomeratic Facies in the Northern Margins of the Arabo-Nubian Shield, *Geological Survey of Israel, Bulletin 87*, 44 pp.
- Wilson, T., 1965. A new class of faults and their bearing on continental drift, *Nature*, **4995**, 343–347.
- Yuval, Z. & Rotstein, Y., 1987. Deep Crustal Reflection Survey in Central Israel, *J. Geodyn.*, **8**, 17–31.
- Zelt, C.A. & Smith, R.B., 1992. Seismic travel time inversion for 2-D crustal velocity structure, *Geophys. J. Int.*, **108**, 16–34.

## APPENDIX

### NVR experiment configuration

Instead of using one multichannel recording system controlling the sources and receivers along the entire spread, something that has been common practice for many years in NVR surveys, a large number of digital seismic stations (Table A1) recorded continuously during source activities. Continuous GPS time monitoring by each recorder and GPS start time measurement of each source allowed the cutting out of the desired recording length for each trace and arrange raw shot gathers. The NVR experiment is to our knowledge the first high-fold, high-resolution vibroseis survey carried out using this modified recording technique. During the roll-along procedure, the first half of each day was used to shift the spread by 3.6 km along the line. In the second half of the day 70 vibrator points (VP) were performed along the inner 7 km of the 18 km spread. These VPs were arranged in blocks of 10 with 50 m spacing alternating with 500 m gaps, which were filled during the previous or following days. In addition, each second and third day respectively, a high-charge explosive shot was fired. Compared to the high-fold vibroseis data the quality of the explosive shots was poor, with no reflections from the lower crust or the Moho. This was probably due to the extremely dry ground. Hence, the NVR explosive data will not be discussed in paper.

### NVR data and processing

Cutting the seismic traces for all channels from the continuously recorded time series using the absolute GPS shot times was partly performed in the mobile field centre for quality control. Arranging all data into uncorrelated, vertically unstacked, shot-sorted traces,

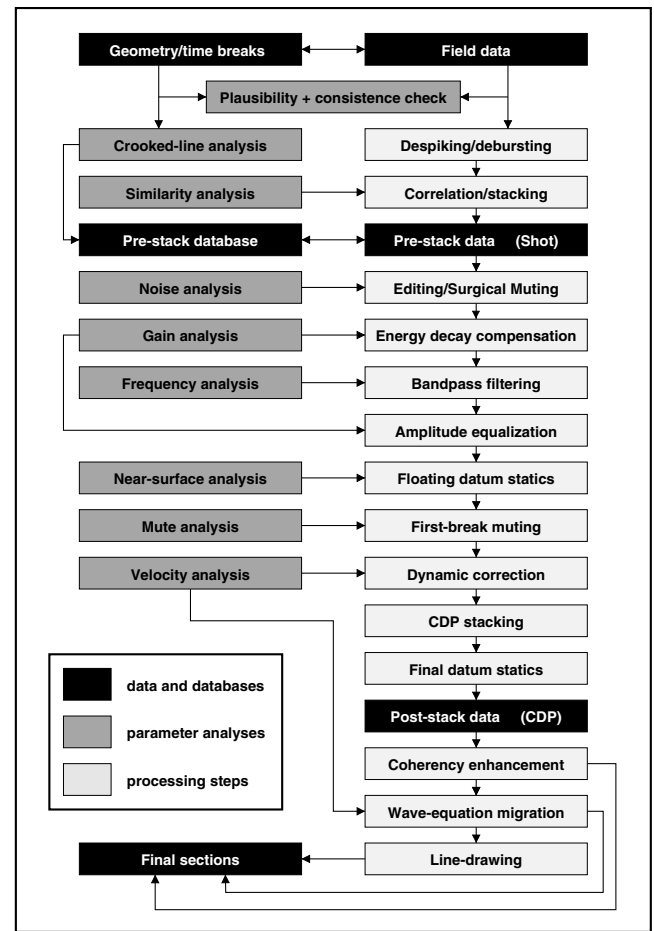
**Table A1.** Acquisition parameters of the NVR experiment.

Recording parameters	
Recording period	1st March–2nd April 2000
Recording area	Sede Boqer (IL) → Ma'an (HKJ)
Recording systems	30 Teledyne PDAS-100 seismological recorders (6 channels + GPS-clock, 1 GigaByte hard disc)
Sample rate	5 ms, continuously recording
Deployment/Data collection	8–14 o'clock
Shooting/Vibrating	14–24 o'clock
Profile length	125 km along geophone line, 102 km along CDP line, 99 km as the crow flies
Profile direction	NW → SE
Receiver specifications	
Number of channels	30 units × 6 channels
Geophone type	Sensor SM 6, 4.5 Hz, vertical
Receiver array	6 per group, linear pattern 15 m in-line
Group spacing	100 m
Block move-up	3.6 km per day
Spread length	18 km
Number of stations	1008
Source specifications	
<i>Vibroseis</i>	(Geophysical Institute of Israel, Lod, Israel)
Number of vibrators	5–6 (260 000 lbs total peak force)
Recording length	24 s sweep + 18 s listening time
Sweep range	10–48 Hz linear
Configuration	asymmetrical split-spread (–9 km . . [–3.4 km . . VP . . 3.4 km] . . 9 km)
Vertical fold	10 vibrations/point, 100 m pattern
Source spacing	50 m
Number of source points	1734 (70 VPs per day)
Subsurface coverage	90 fold
Data amount	17 260 sweeps × 180 channels × 8600 samples = 3.1 million traces = 106.8 Gbyte
<i>Explosive</i>	(Site Group, Chemical Mining Ind., Amman, Jordan; Geophysical Institute of Israel, Lod, Israel)
Charge	100 kg per shot in 30 m depth
Recording length	60 s
Configuration	asymmetrical split-spread shooting (2:3, 3:2)
Shotpoint spacing	alternating 7.2 km and 10.8 km
Number of shots	10
Subsurface coverage	single fold
Data amount	10 × 180 channels × 12 000 samples = 87 Mbyte

archiving in standard SEG Y format and further processing was carried out at the GFZ using Landmark's ProMax software. The principal processing sequence is given in Table A2 and will now be discussed in detail.

The first step was the validation of the data, the geometry and the absolute time-bases. After consistency and plausibility checks of the data a Common Depth Point (CDP) geometry, based on a crooked-line design, was generated, as due to the rough terrain and other boundary conditions (natural protection and military areas, border crossing) a straight line was impossible. The crooked-line nature of the profile results in a laterally strongly scattered CDP distribution. Therefore the subsurface traces, which numbered more than 300 000, were projected onto a smoothly curved 'reflection'

**Table A2.** Processing chart of the NVR data set.



line (Fig. 2b). Before this, however, all VP gathers were cross correlated with the pilot sweep and vertically summed using a diversity stacking algorithm, which weights the sum by the individual trace similarities, resulting in an efficient noise reduction. The final horizontal subsurface coverage is 90-fold with a CDP trace spacing of 25 m.

After application of a DC removal to correct for the amplifier drift of the instruments (no filters had been applied in the field except the anti-alias filter) some effort had to be made to deal with numerous bad or partly disturbed traces affected by several types of both source-generated and other noise amplitudes or wave trains. Due to the large number of traces an automatic pre-first-break/post-first-break energy threshold had to be used to distinguish between good and bad traces. This resulted in about 20 per cent of the traces being discarded. The heterogeneous character of the data is illustrated in Figs A1(a) and (b), where two adjacent common receiver gathers, located only 100 m apart, show quite different images, especially in the lower crust (10 to 12 s). The same phenomenon can also be observed in adjacent common shot point or common midpoint gathers. The stacking result after 'bad' traces and gathers have been discarded (Fig. A1c), shows the signal/noise enhancement due to the high-fold coverage. Moreover, most of the sweeps produced a strong air-blast wave visible along the entire spread and therefore a sharp 'surgical muting' was necessary. Numerous spikes and singular noise bursts, probably induced by electromagnetic effects could be detected with an automatic despiking/debursting algorithm and were removed by zeroing the affected time intervals before vibroseis correlation.

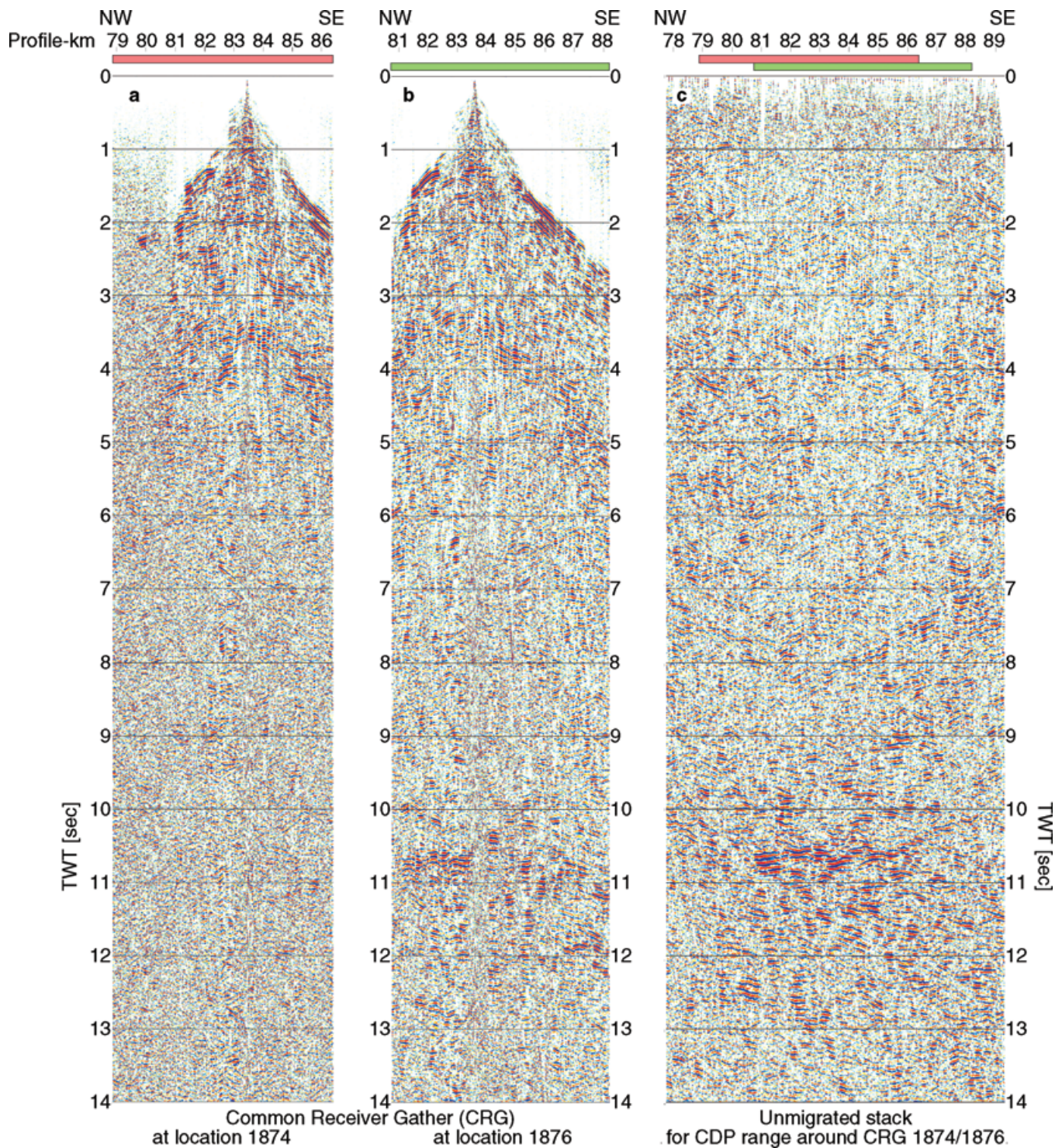


**Figure A1.** (a) Common Receiver Gather (CRG) at 83.4 km along the NVR profile with bad S/N ratio, (b) CRG at 83.5 km along the NVR profile with good S/N ratio, (c) 11 km wide CDP stack with strong reflections from the lower crust (10 to 12 s). The locations of the CRGs are marked at the top of the stack.

Time and space-variant, zero-phase band-pass filters were determined and applied to restrict the amplitude spectra to the signal frequencies between 10 and 50 Hz. For the reflected wavefield, however, the main signal frequencies are on average between 10–30 Hz, on rocky ground up to 10–40 Hz and on sandy ground between 10–20 Hz. The main signal frequencies along the NVR profile (Fig. A2) seem to be connected to the geology and near-surface conditions.

The highest frequencies occur about 20 km west of the AF where Eocene limestone and chalk crop out at the surface, while the lowest occur around and east of the AF which is an area covered by alluvium and sand dunes. Some faults seem to be indirectly imaged by sudden frequency changes.

Amplitude scaling in time and space was a compromise between preserving the ‘true amplitudes’ that ideally represent the

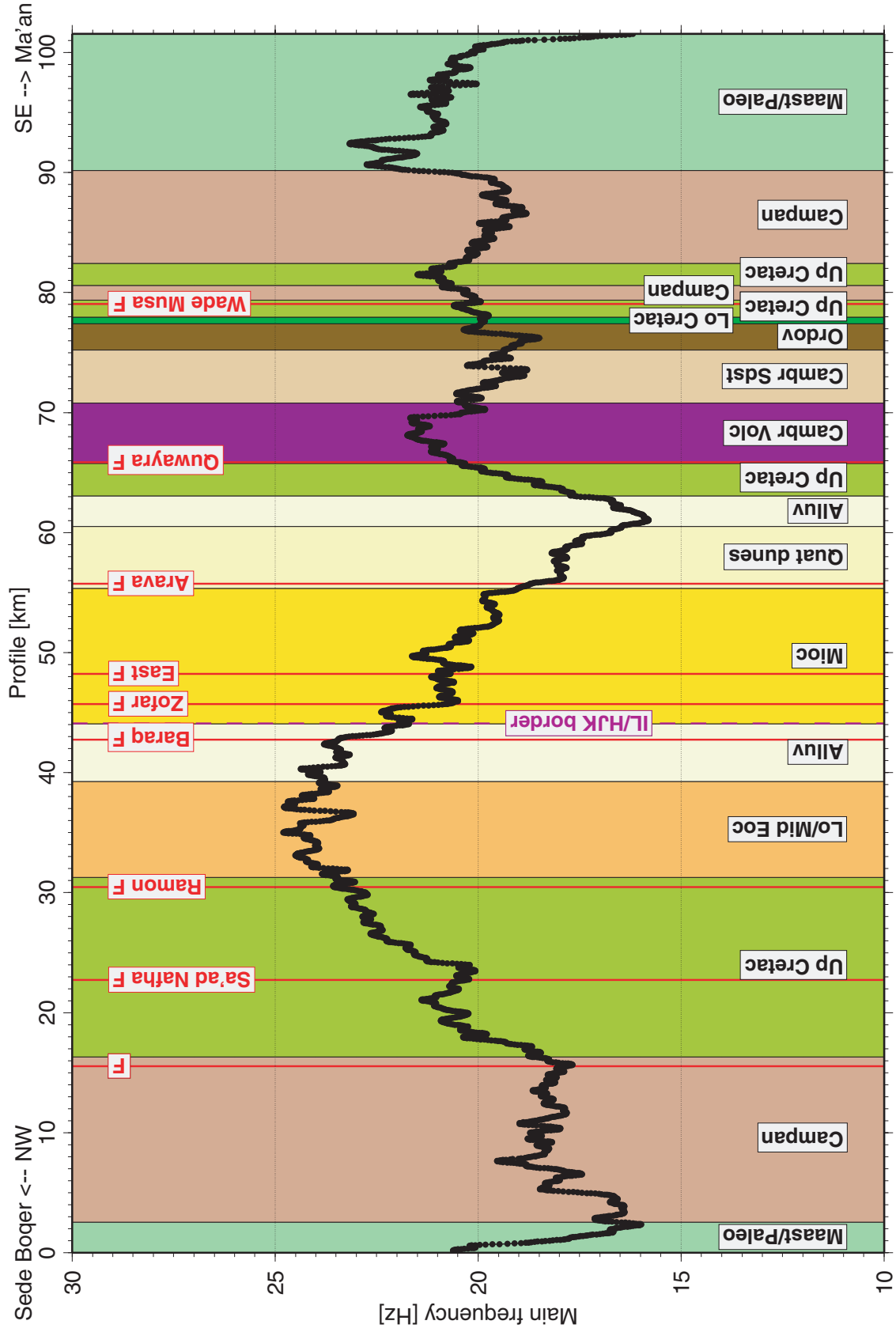


Figure A2. Main signal frequencies recorded along the NVR profile with the stratigraphy of the geological units indicated by background colours, see also Fig. 2(b).

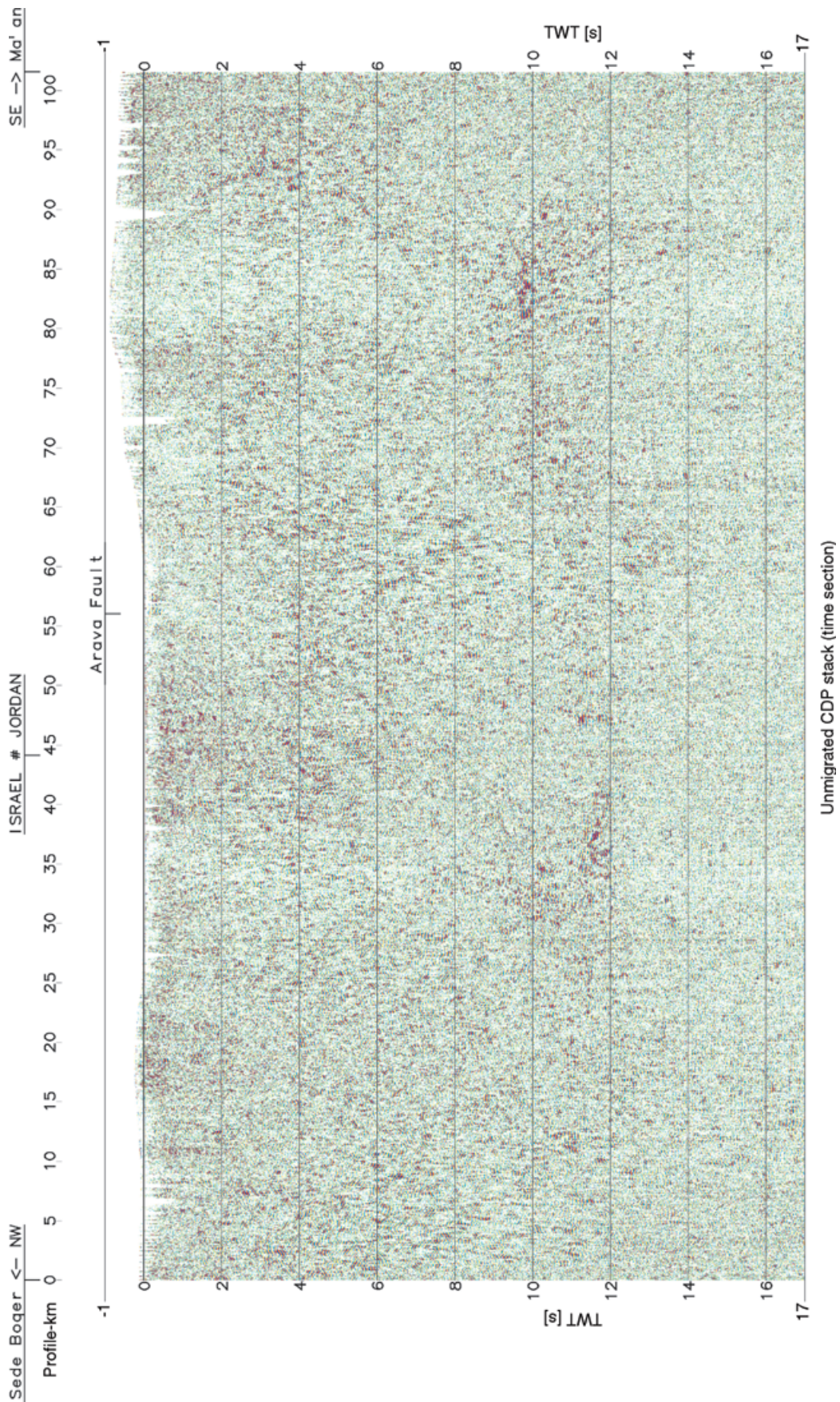


Figure A3. Unmigrated Common Depth Point stack along the NVR profile.

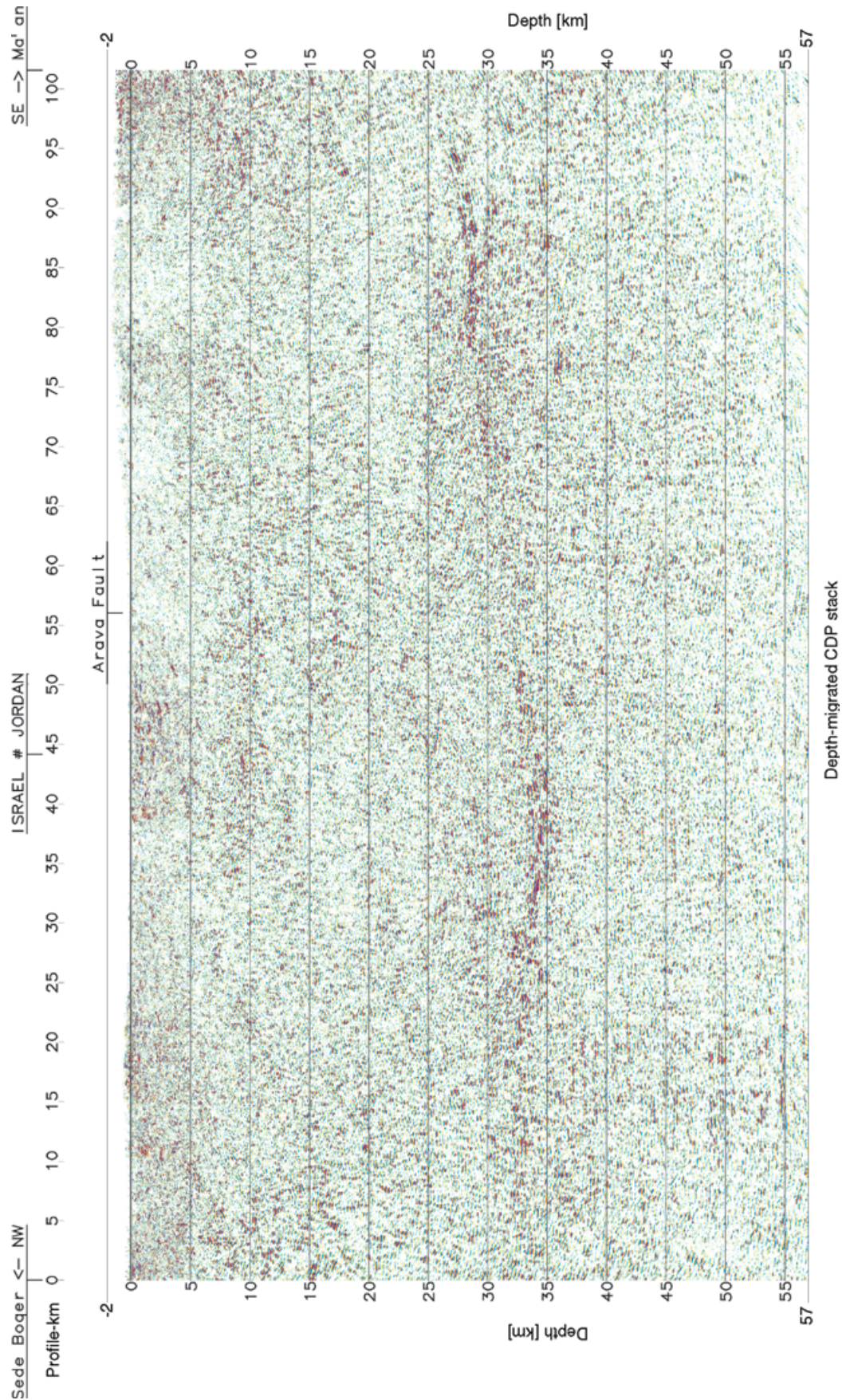


Figure A4. Depth-migrated Common Depth Point section along the NVR profile.

reflectivity of the subsurface and suppressing all noise amplitudes and those amplitudes that carry no subsurface information at all, i.e. geophone coupling, source strength, near-surface heterogeneities, superimposed non-source generated noise etc. These parameters are usually unknown and, especially in land seismic, extremely heterogeneous. To account for the wave front spreading a spherical divergence correction via an analytical gain curve was applied. In addition, some automatic gain control in the form of a large-window feed-back AGC to correct for remaining vertical amplitude level variations was necessary, as well as some horizontal trace level equalization based on a crustal-scale time-window. Careful parameter selection ensured preservation of the relative amplitude dynamics and also met the necessary input presumptions for the following processes, i.e. the basic stacking condition of summing only similar and equivalent traces.

No additional measurements for resolving the near-surface conditions, such as accompanying short-refraction lines, were carried out. Therefore, only elevation-based static time corrections using an average correction velocity were calculated to change from the actual source and receiver positions to a common datum. Following these corrections, certain time delays still remained in the data, obviously caused by variable near-surface low velocity layers, especially in the vicinity of sand dunes and gravel fields. Automatic determination of residual statics using cross correlation methods was not successful, probably due to missing marker horizons in combination with the generally low bandwidth character of the data. Due to the large elevation differences (1750 m) the total static correction was split into two portions. The smaller portion from the actual elevations to an intermediate, so-called 'floating' datum, following the smoothed topography, was applied before normal move-out (NMO) correction. The much larger part from the floating to a fixed datum (sea level) was applied after CDP (Common Depth Point) stack-

ing. Thus more homogeneous and realistic stacking velocities are obtained along the line. Finally, the zero-time (or depth) in the depicted final seismic sections corresponds to sea level and, therefore, the data at higher elevations occur at negative times or depths.

First breaks, usually diving refraction events, must be removed as well as reflection events at wide-angle distances since they do not follow the hyperbolic reflection formulae. So-called top muting, individually analysed for numerous VPs before dynamic correction, was applied, zeroing trace portions offset-dependently to enable constructive stacking of near-vertical reflection events neglecting the dynamically uncorrectable, non-hyperbolic far-offset portions.

Dynamic time corrections by NMO velocity analyses turned out to be difficult and ambiguous due to unclear stacking semblance maxima despite the high CDP fold. Therefore, a  $v_{rms}$ -TWT background-model was derived from turning-ray tomographic inversion for the upper time range and from the wide-angle data along the WRR line for the lower time range to find the appropriate NMO velocities for the NVR data. Nevertheless, the results of the NMO-corrected and stacked zero-offset data tend to remain unsatisfactory in some regions, revealing that the basic stacking condition, the alignment of signals with an error less than the dominant wavelength, might not have been sufficiently met. The reasons for this are assumed to be strong lateral scattering errors of the CDPs, incomplete near-surface related static corrections as well as high absorption of higher frequencies, disabling a better signal-to-noise improvement during stacking.

In deep-crustal seismic, multichannel coherence enhancement techniques play a significant role, since lateral coherence is a much higher criterion for discriminating signal from noise than amplitudes. The Fresnel zones are wide enough for dip-analysis apertures consisting of a sufficient number of traces. In general, the two

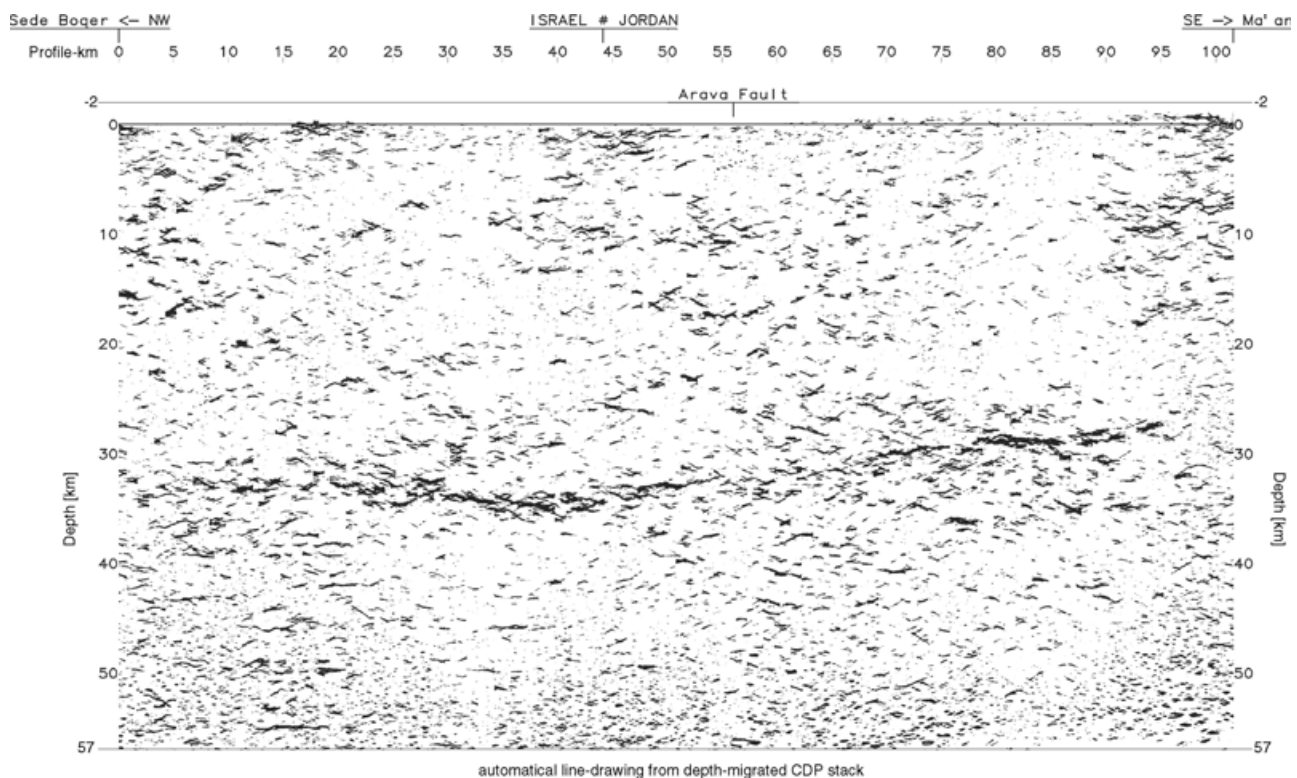


Figure A5. Automatic line drawing of depth-migrated Common Depth Point section along the NVR profile.

important input assumptions for most multichannel processes that sample the data horizontally are equidistant traces and no spatial aliasing. An event-enhancement algorithm based on limited-aperture  $\tau - p$  transforms with semblance weighting gives proper results concerning random noise suppression and lateral, dip-preserving coherence increase. Although application before migration requires caution, it was very efficient for these data, since reflectivity was significantly emphasized and noise was substantially suppressed. Fig. A3 shows the unmigrated stacked section in the TWT-domain.

In general, automatic migration is difficult to handle in deep seismics, when migration operators become large (tens of kilometres) for greater depths at high velocities creating considerable 'smiles' in the lower parts of the sections, since the basic assumption (noise-free, true-amplitude zero-offset input) usually cannot be properly met. Several wave-equation migration methods such as frequency-wavenumber, finite difference (FD) and Kirchhoff summation schemes were therefore tested in the time and depth domains to obtain a spatially 'true' image of the subsurface showing all reflections with the correct dip at the correct depth. A  $50^\circ$  finite-differences depth approach using explicit FD extrapolators, with a

smoothed interval-velocity depth model calculated from the WRR-velocities, turned out to be the best compromise between clear and robust imaging and minimal 'smile'-like artefacts down to depths of 60 km. Fig. A4 shows the migrated stacked section in the depth domain.

Depiction of large seismic transects (NVR: 101 km long,  $\Delta x$  25 m, and 60 km deep,  $\Delta z$  6.25 m, i.e.  $\sim 4050 \times 9600$  depth points) is a challenge, especially if the objective is to use original seismic data instead of manually interpreted line drawings. Therefore automatic line-drawing techniques were used to provide the most objective representation of coherent reflectivity. Here, we calculated perigram traces (the reflection envelope via the Hilbert transform with the suppression of the DC component) of the final migrated section and applied an algorithm based on semblance weighting of locally  $\tau - p$  transformed sliding data-subsets. This should guarantee the restriction to the dominant features of the section, including the correct handling of conflicting dips. Fig. A5 shows the automatic line drawing in the depth domain. An interpretation of the main features seen in Fig. A5 is given together with the discussion of the WRR data.